Article

Nanoparticle Charge and Size Control Foliar Delivery Efficiency to Plant Cells and Organelles

Peiguang Hu, Jing An, Maquela Matamis Faulkner, Honghong Wu, Zhaohu Li, Xiaoli Tian, and Juan Pablo Giraldo

ACS Nano, **Just Accepted Manuscript** • DOI: 10.1021/acsnano.9b09178 • Publication Date (Web): 06 Jul 2020

Nanoparticle Charge and Size Control Foliar Delivery Efficiency to Plant Cells and Organelles

Peiguang Hu[1‡], Jing An[2,1‡], Maquela M. Faulkner[1], Honghong Wu[1,†], Zhaohu Li[2], Xiaoli Tian[2], Juan Pablo Giraldo[1]*

[1]Department of Botany and Plant Sciences, University of California, Riverside, California 92521, USA

[2]State Key Laboratory of Plant Physiology and Biochemistry, College of Agronomy and Biotechnology, China Agricultural University, Beijing 100193, China

[‡]These authors contributed equally.

[*]Corresponding Author: juanpablo.giraldo@ucr.edu

Abstract

Fundamental and quantitative understanding of the interactions between nanoparticles and plant leaves is crucial for advancing the field of nano-enabled agriculture. Herein, we systematically investigated and modeled how zeta potential (-52.3 mV to +36.6 mV) and hydrodynamic size (1.7-18 nm) of hydrophilic nanoparticles influence delivery efficiency and pathways to specific leaf cells and organelles. We studied interactions of nanoparticles of agricultural interest including carbon dots (CDs, 0.5 and 5 mg/mL), cerium oxide (CeO_2, 0.5 mg/mL) and silica (SiO_2, 0.5 mg/mL) nanoparticles with leaves of two major crop species having contrasting leaf anatomies: cotton (dicotyledon) and maize (monocotyledon). Biocompatible CDs allowed real-time tracking of nanoparticle translocation and distribution *in planta* by confocal fluorescence microscopy at high spatial (~200 nm) and temporal (2-5 min) resolution. Nanoparticle formulations with surfactants (Silwet L-77) that reduced surface tension to 22 mN/m were found

to be crucial for enabling rapid uptake (< 10 min) of nanoparticles through the leaf stomata and cuticle pathways. Nanoparticle-leaf interaction (NLI) empirical models based on hydrodynamic size and zeta potential indicate that hydrophilic nanoparticles with less than 20 and 11 nm for cotton and maize, respectively, and positive charge (> 15 mV), exhibit the highest foliar delivery efficiencies into guard cells (100%), extracellular space (90.3%), and chloroplasts (55.8%). Systematic assessments of nanoparticle-plant interactions would lead to the development of NLI models that predict the translocation and distribution of nanomaterials in plants based on their chemical and physical properties.

Keywords

carbon dots, cerium oxide nanoparticles, silica nanoparticles, surfactant, crops, agriculture.

The rapid growth in human population will require about 60% increase or more in food production by 2050 relative to 2005-2007.[1] However, recent increases in annual crop yield rates from 2005 to 2014 are significantly lower than those in preceding years[2] and far behind those required to secure the food demand in 2050.[3–5] Furthermore, climate change is exacerbating the frequency and intensity of major environmental stresses such as drought, heat, and pathogen infections that negatively impact crop productivity.[6–8] Agricultural production faces many other challenges including largely inefficient use of resources such as fertilizers, pesticides, and herbicides used for improving crop yields. About 40-90% of these agrochemicals are lost to the environment and never reach their target in plants.[9–11] This unsustainable use of resources leads to not only massive economic and energy losses but also significant negative environmental pollution.[12–15] Improvement in crop yields will require convergent and multidisciplinary approaches for enhancing plant tolerance to environmental and pathogen stresses and the efficient use of resources.

Nanoscale materials exhibit distinct physical and chemical properties that enable them to act as unique tools for research and development of agricultural technologies.[16–21] Nanomaterials have been demonstrated to improve plant tolerance to environmental[22–24] and biotic stresses,[25–27] to enhance agrochemical delivery efficiency,[17,28–32] to act as sensors that monitor plant signaling

molecules and pollutants in the environment,[33–37] and to facilitate gene delivery to plant nuclear and plastid genomes.[38,39] Currently, the main strategies employed for nanomaterial delivery to plants in the field are soil drenching,[40–44] feeding/injection,[22,24,28,33–35,38,39,45–48] and foliar delivery.[46–60] Most nanoparticles applied to soil are not taken up by plants due to nanomaterial heteroaggregation in soil, soil runoff, or root biological barriers.[41,61–65] Although feeding/injection methods are highly efficient to deliver nanomaterials directly into plants, they are labor intensive.[22,24,28,33–35,38,39,49] Foliar topical delivery provides an efficient and scalable approach for directly interfacing nanomaterials with plants. However, a poor understanding of how nanoparticle chemical and physical properties control the translocation, distribution, and attachment of nanomaterials in plant leaves limits the use of nanotechnology in nano-enabled agriculture.

Previous studies on nanoparticle uptake in plant protoplasts (lacking cell walls)[66] and isolated chloroplasts[28] *in vitro* have discovered the role that zeta potential and size play on nanoparticle translocation across plant plasma membrane and organelle lipid bilayers. These studies report that positively or negatively charged nanoparticles with zeta potential magnitudes higher than 20 or 30 mV (Smoluchowski approximation) are more likely to be taken up by plant cell or chloroplast membranes, respectively, whereas more neutral nanomaterials are not able to penetrate plant lipid bilayers. As the size of the nanoparticle decreases, larger magnitude of zeta potential is needed for enabling translocation across lipid membranes. However, a systematic and modeling study of how charge and size influence nanoparticle transport *in vivo* from the leaf surface (epidermis) into leaf cells and their organelles has not been performed. *In vivo* nanoparticle translocation across leaves requires them to cross not only cell and organelle lipid membranes but also the leaf cuticle, stomatal pores, and cell walls (Figure 1a). The leaf surface is formed by a waxy layer called the cuticle containing nanoscale (~2 nm) hydrophilic pores,[49,67–71] and micron scale stomatal pores. The cuticle and stomata are main pathways for nanomaterial delivery to plant leaves. Inside leaves, the cell wall is a biological barrier with both hydrophobic and hydrophilic components,[72] with a reported pore size less than 13 nm,[73] and unequal distribution of fixed negative charges.[74,75] The upper size exclusion limit for transport of nanoparticles through plant cells and the impact of charge on nanoparticle translocation across these cells remains unclear.[75–77]

Herein, we systematically investigated and modeled how nanomaterial zeta potential and hydrodynamic size impact the interactions of hydrophilic nanoparticles with leaf cell surfaces and organelle membranes of chloroplasts, key plant photosynthetic organelles. We designed and synthesized ten types of nanoparticles including fluorescent carbon dots (CDs), CeO_2 (NC) and SiO_2 (SN) nanoparticles (NP) to study how nanoparticle properties affect their translocation across leaf biological barriers and their distribution in leaf cells. CDs are bright and fluorescent nanomaterials with high quantum yield, high resistance to photobleaching, tunable emission range,[78–81] and facile surface functionalization. These biocompatible nanomaterials[82–84] have been used for improving plant growth and disease resistance, and bioimaging in whole plants.[60,85,86] The unique optical properties of CDs are optimal for high spatial and temporal resolution imaging by confocal microscopy[84] and studying nanoparticles interactions with leaf biological barriers. CeO_2 NPs acting as catalytic antioxidants have been delivered to chloroplasts in plant model systems to improve plant tolerance to stresses including heat, chilling, high-light,[24] and salinity.[22] The SiO_2 NPs have been reported to act as gene and agrochemical delivery platforms,[87–90] and to improve crop yield.[90–92]

We tested the overarching hypothesis that nanomaterial zeta potential and size determine the translocation and distribution of nanoparticles in leaf cells of plants with contrasting leaf anatomies, cotton (*Gossypium hirsutum* L.) and maize (*Zea mays* L.), corresponding to the major plant taxa of dicotyledons and monocotyledons, respectively. Only one previous study has compared nanoparticle interactions between dicotyledons and monocotyledons, reporting differences in translocation from roots to shoots.[93] To accomplish this study's overarching goal, 1) we synthesized and characterized CDs, CeO_2, and SiO_2 NPs with specific fluorescent emission properties, positive or negative zeta potential, and specific hydrodynamic diameters; 2) we developed nanoparticle formulations containing surfactants and studied the influence of surface tension on enabling rapid and efficient foliar nanoparticle delivery for potential nano-enabled agricultural applications; 3) we developed approaches for imaging nanoparticle translocation in leaves by confocal fluorescence microscopy at high spatial and temporal resolution; 4) we assessed how nanoparticle zeta potential and hydrodynamic size influence their distribution in leaf cells and organelles including stomatal guard cells, extracellular space and

chloroplasts; and 5) we created nanoparticle-leaf interactions (NLI) empirical models based on nanomaterial zeta potential and hydrodynamic size for designing nanoparticles with higher delivery efficiency into specific leaf cellular compartments.

Results and Discussion

Characterization of plant leaves with different anatomy

The cuticle and stomata are the two main pathways of nanomaterial entry through the leaf epidermis into the mesophyll (Figure 1a). Inside leaves, nanomaterials can translocate across extracellular (apoplastic) and/or intracellular (symplastic) pathways in the mesophyll. To enter leaf mesophyll cells and chloroplasts from the extracellular space (apoplast), nanoparticles have to cross main plant biological barriers such as the cell wall, plasma and organelle membranes. Leaf anatomical differences between maize (monocot) and cotton (dicot) leaves are illustrated in scanning electron microscopy (SEM) images of the leaf surface (Figure 1b), and light microscopy images of leaf cross-sections (Figure 1c). The density of dumbbell shaped stomata in the leaf epidermis of maize, 34.3 ± 4.6 mm^{-2}, is eight times lower than that of kidney shaped stomata in cotton leaves, 258.4 ± 32.2 mm^{-2} ($P < 0.01$, Figure S1a). In contrast, the stomatal length in maize leaves, 34.3 ± 0.4 μm, is more than twice higher than that of cotton leaves, 13.4 ± 0.8 μm ($P < 0.001$, Figure S1b). Both palisade and spongy mesophyll cells can be identified in the leaf mesophyll of cotton leaves, whereas only one type of mesophyll cells characteristic of maize leaves can be observed. In the cotton leaf, the palisade mesophyll cells are closely packed side-by-side below the adaxial (upper) leaf side, leaving little extracellular air space in between them except underneath the stomatal pores. The spongy mesophyll cells in cotton leaves are sparsely distributed on the abaxial (lower) leaf side creating large extracellular air spaces. In contrast, tightly packed mesophyll cells were observed in the maize leaf cross-section, leaving small air spaces underneath the stomatal pores. These leaf anatomical traits for cotton and maize are characteristic of dicotyledonous and monocotyledonous plant species, respectively.[94] Leaf autofluorescence spectra for crop leaves were independent of the excitation wavelength (405, 476, and 514 nm) used for confocal microscopy imaging (Figure S2). However, variations in

chlorophyll a/b ratios in cotton and maize leaves can result in slight differences in pigment autofluorescence spectra between these plant species [95,96] (Figure 2c and S2).

Nanoparticle chemical and physical properties

Hydrodynamic size measurements by DLS (dynamic light scattering) confirmed the synthesis of CDs, CeO_2, and SiO_2 nanoparticles with average size from 1.7 to 18.0 nm (Table S1, average ± standard deviation) (Figure 2a). Representative TEM images show the core size of nanoparticles in similar range from 1 to 15 nm (Figure S3). Nanoparticle zeta potentials from -52.3 mV to +36.6 mV (Table S1, average ± standard deviation) were significantly different except between SA-CD6 and DiI-PNC11, DiI-PNC2 and FITC-SN18 ($P < 0.05$) (Figure 2b). Zeta potential of PEI-CDs (polyethyleneimine coated CDs), and DiI-ADNCs (DiI labeled aminated dextran coated NC) are positive due to surface functionalization with amine-rich coatings. In contrast, SA-CDs (succinic anhydride modified PEI-CDs), DiI-PNCs, [DiI labeled poly (acrylic acid) coated NCs], and FITC-SN18 (FITC labeled SN) exhibit negative zeta potentials because of abundant carboxyl or silanol groups on the surface. The surface chemical composition of nanoparticles was confirmed by Fourier-transform infrared spectroscopy (FTIR) showing the successful functionalization of the nanomaterial surface by different coatings (Figure S4). We designed the nanoparticles for high resolution confocal microscopy imaging by minimizing their fluorescence emission overlap with leaf autofluorescence (Figure 2c and S2). The nanoparticle excitation wavelengths in both confocal microscopy and *in vitro* fluorescence measurements were set at 405, 514, and 476 nm for CDs, DiI-NCs and FITC-SN18, respectively, close to the absorption maximum in UV-vis absorption spectra (Figure S5). Nanoparticle fluorescence emission ranges from 410 to 600 nm for CDs, 550 to 650 nm for DiI-NCs, and 500 to 600 nm for FITC-SN18, with no significant overlap with the leaf autofluorescence from 670 to 800 nm (Figure 2c and S2).

Influence of formulation surface tension on nanoparticle foliar delivery

Surfactants are widely used in agrochemical formulations for improving contact with plant surfaces.[97–102] To the best of our knowledge there are no studies assessing their role and impact on nanoparticle foliar delivery efficiency. The leaf surface of cotton and maize plants was interfaced with CDs of different size and charge that were previously suspended in nanoparticle

formulations with surface tension about 30 mN/m or 22 mN/m by adding Triton X-100 or Silwet L-77, respectively. Nanoparticles did not affect the formulation surface tension and maintained formulation pH values (5.3 - 8.5) within the plant physiological range (pH 5-8) (Figure S6). Leaf uptake was determined as fluorescence of CDs observed in the leaf extracellular space, mesophyll cells, or both. Confocal fluorescence microscopy images of leaves exposed to CDs (after 3 h) (Figure 3 and S7) indicated that formulations containing Silwet L-77 with relatively low surface tension allowed CDs of 2-6 nm size to penetrate through the leaf surface. In contrast, formulations with Triton X-100 having a higher surface tension only allowed CDs of 2 nm size to enter maize leaves (Figure 3 and S7). Therefore, we assessed nanoparticle foliar translocation and distribution using Silwet L-77, the more effective surfactant. Non-surfactant-containing formulations had poor wettability on the leaf surface, forming semi-spherical or spherical drops on cotton and maize leaf surfaces. Confocal microscopy images taken from leaf tissues right underneath the area of nanoparticle exposure indicated that no CDs suspended in water without surfactant translocated inside leaves (Figure S8). Similarly, Avellan *et al.* applied gold nanoparticles in aqueous solution without surfactant on wheat leaves and reported significantly reduced amounts (~20%) of hydrophilic gold nanoparticle (3 nm, zeta potential -69.2 mV, concentration 10 mg-Au/L) adhesion to wheat leaves (2 h after exposure), compared to 100% for amphiphilic gold nanoparticles (3 nm, zeta potential -56.8 mV, concentration 10 mg-Au/L).[103]

These results were further confirmed with 3D images created from confocal microscopy z-stack images (2 μm z-axis resolution and 225-285 nm x-y resolution, Leica SP5) of cotton and maize leaves treated with 10 different types of fluorescent nanoparticles in formulations with Silwet L-77 (Figure S9). Nanoparticles in surfactant formulations exhibited high stability (Figure S10). Fluorescent dye molecules strongly associated with the cerium oxide and silica nanoparticles and no dissociation occurred even in the presence of Silwet L-77 (Figure S11). In cotton, all the nanoparticles with hydrodynamic size up to 18 nm penetrated the leaf surface (Figure S9a). In contrast, nanoparticles with hydrodynamic size larger than 8 nm were not permeable through the maize leaf surface (Figure S9b). The surfactant concentrations used in this study were similar to those used in actual agricultural formulations[98,99] and do not have a detrimental impact on leaf health in cotton and maize (Figure S12). The CD formulations in Silwet L-77 as surfactant were designed to be biocompatible with plants by monitoring the impact of formulation exposure on

leaf chlorophyll content. No significant differences of leaf chlorophyll content were observed between control untreated leaves and those interfaced with CDs suspended in formulations with Silwet L-77 (Figure S12). Chlorophyll content indexes measured with a SPAD meter before and 3h after exposure of leaves to nanoparticles were similar (Figure S12) indicating that nanoparticle exposure does not interfere with SPAD meter readings.

High spatial and temporal resolution imaging of nanoparticle translocation in leaves *in planta*

Leaves of intact plants mounted on a confocal microscope were treated with positively or negatively charged CDs, PEI-CD2, PEI-CD6, SA-CD2, and SA-CD6 with hydrodynamic sizes of 2 and 6 nm, previously suspended in formulations with Silwet L-77. Z-stack images were collected every 2 to 5 min from the leaf surface to the mesophyll (2 μm z-axis resolution and 206 - 233 nm x-y resolution, Zeiss 880), generating time-lapse videos of nanoparticle pathways of translocation across leaves in real-time and *in planta* (Video S1, S2, S5, S6, S9, S10, S13, and S14). Snapshots of our real-time confocal microscopy videos within the leaf epidermis and mesophyll layers, and the reconstructed 3D images from z-stacks suggest different pathways of foliar entrance for PEI-CD2, SA-CD2, PEI-CD6, and SA-CD6 in cotton and maize leaves (Figure 4 and S13-S15, Video S3, S4, S7, S8, S11, S12, S15, and S16). All CDs translocated across the cotton leaf surface through both stomatal and cuticular pathways (Figure 4 and S13-S15, Video S1, S3, S5, S7, S9, S11, S13, and S15). In contrast, stomata were the main pathway of entrance for all the four CDs in maize leaves, highlighting potential differences of nanoparticle translocation between monocots (maize) and dicots (cotton) (Figure 4 and S13-S15, Video S2, S4, S6, S8, S10, S12, S14, and S16). The presence of nanoparticle fluorescence signals in stomatal guard cells or pores in both plant species indicates translocation through the stomatal pathway (Figures 4 and S13-S15). Species dependent differences in initial nanoparticle translocation through either stomatal pores (Figure 4, maize), guard cells or both (Figure 4, cotton) are interesting subjects of future studies on translocation of nanoparticles within stomatal structures. Nanoparticle fluorescence is also observed around the epidermal cell boundaries in cotton and to a much less extent in maize (Figures 4, S13-S15) suggesting that nanoparticles are distributed within anticlinal cell walls rich in hydrophilic pores.[73] The hydrophilic pores in the

cuticle have been reported to be smaller than 2 nm[67–69] representing a likely size exclusion limit factor for larger hydrophilic nanoparticles.

For both cotton and maize plants, the CDs rapidly entered the leaves within only a few minutes after nanoparticle exposure and localized within different cellular intracellular and extracellular compartments in the leaf mesophyll within 1 hr. Nanomaterials can rapidly penetrate plant cell membranes *via* non-endocytic pathways[24,104] by disrupting lipid bilayers.[28,66] Previous studies have reported transport of nanoparticles across the leaf surface but in significantly longer time frames of several hours or days after nanoparticle exposure.[71,103] Avellan *et al.* recently reported using X-ray mapping that hydrophilic citrate-Au NPs, especially those about 3 nm in size, are preferentially taken through the stomatal pathway in wheat (monocot).[103] Surface chemistry also influences gold nanoparticle (AuNPs) translocation through the leaf surface.[103] Coating Au NPs with polyvinylpyrrolidone (PVP, an amphiphilic polymer) led to complete uptake through the leaf, while the hydrophilic citrate coating left a large fraction of Au NPs on the leaf surface.[103]

Impact of nanoparticle charge and size on their distribution in leaf cells and organelles

We assessed by confocal fluorescence microscopy how hydrodynamic size and zeta potential of CD, CeO_2 and SiO_2 NPs affect their distribution in leaf cells and organelles including guard cells, extracellular space, and chloroplasts (Figure 5 and S16-S19). Guard cells are important cellular structures regulating CO_2 and H_2O gas exchange,[105,106] and the gates for plant pathogen infections.[107] The extracellular space exhibits marked differences between cotton and maize (Figure 1) and is characterized by a low pH (~5)[108] that could significantly influence transformations of nanoparticles for agrochemical delivery. Translocation of nanoparticles into cells and photosynthetic organelles such as chloroplasts requires movement across major plant cellular barriers such as the cell wall, plasma membrane and organelle lipid bilayers. The colocalization rate of nanoparticles with chloroplasts (Figure 5b) was analyzed by identifying overlapped fluorescence peaks in six transects of ROI (region of interest) equidistantly separated in confocal image overlays (See methods) as described in previous studies.[24,109] The chloroplast colocalization rate with nanoparticles assessed by ROI analysis was confirmed by Manders' overlap coefficient analysis[110] based on the percentage of chloroplast pixels overlapping with nanoparticle pixels. The colocalization rates based on ROI analysis and Manders' overlap

coefficients were positively correlated ($P < 0.0001$) (Figure S20). Nanoparticles were localized in the extracellular space of the leaf mesophyll (Figure 5c) as the nanoparticle occupied area outside the cell boundary delineated by chloroplasts in confocal microscopy imaging (Figure S21).[111–113] Nanoparticles were identified in guard cells by performing z-stacks as described above from the stomata upper surface in the leaf epidermis into the leaf mesophyll (Figure 5d). As shown in the orthogonal views of confocal microscopy images (Figure 5d, after 3 h exposure), the nanoparticle fluorescence is observed within guard cells and also in stomatal pores.

The impact of charge and size on nanoparticle leaf cellular distribution was quantitatively assessed as the percentage of guard cells, extracellular space area, or chloroplasts containing nanoparticles (Figure 6). We identified nanoparticles with efficient delivery to guard cells, extracellular space, or chloroplasts as those with colocalization rates above the average rates minus SE (standard error) of all nanoparticles tested (Figure 6, see methods). Most nanoparticles with hydrodynamic size up to 16 and 8 nm, in cotton and maize, respectively, exhibited above average colocalization with leaf guard cells, and nanoparticles with larger hydrodynamic size showed significantly lower delivery efficiencies ($P < 0.05$) (Figure 6a). This indicates a limitation of nanoparticle penetration into guard cells due to the cell wall size exclusion limit that is likely plant species specific. Patterns of nanoparticle localization in the extracellular space were complex and varied depending on plant species, charge and size (Figure 6b). In cotton, all positively charged nanoparticles with a size up to 12 nm were found efficiently localized in the extracellular spaces but most negatively charged nanoparticles were found at significantly lower levels in this compartment ($P < 0.05$). In contrast, nanoparticles were efficiently delivered to extracellular space in maize when the hydrodynamic size was 6-8 nm for positively charged nanoparticles and 2-6 nm for most negatively charged nanoparticles. Nanoparticles with hydrodynamic size smaller than 12 and 6 nm for cotton and maize, respectively, tend to have above average delivery efficiency to chloroplasts in leaf mesophyll cells ($P < 0.05$). In both crop species, the percentage of chloroplasts colocalized with nanoparticles was higher in nanoparticles with positive zeta potential compared to their negatively charged counterparts ($P < 0.05$) (Figure 6c). Although colocalization rates with chloroplasts in maize mesophyll cells were above average for positively charged nanoparticles under 6 nm in size ($P < 0.05$), the colocalization

values with chloroplasts were low and did not surpass 30%. The plant cell wall is negatively charged[74] which can have a higher affinity with positively charged nanoparticles and act as a cation exchange membrane facilitating their passive translocation across cell walls.[75–77] Moreover, it has been reported that cationic nanoparticles exhibit higher cellular uptake because of the negative transmembrane electrical potential with respect to the exterior of the cell.[114,115] The topical foliar delivery of nanoparticles suspended in surfactants and without external mechanical aid used in this study may also play a role in promoting the delivery of positively charged nanoparticles across cell wall and membranes. We have previously observed and reported a higher delivery efficiency of negatively charged CeO_2 NPs to *Arabidopsis* chloroplasts by needleless syringe infusion through the leaf lamina.[24] Overall these results indicate that nanoparticle delivery efficiency to leaf cells and organelles are influenced by zeta potential and limited by the cell wall pore size in a plant species dependent way.

Leaf anatomical differences in cotton and maize leaves could explain differences in nanoparticle foliar delivery efficiency. The smaller extracellular air spaces and tightly packed mesophyll cells in maize leaves contribute to reduce the cell surface area exposed to nanoparticles entering through stomatal pathways (Figure 1). Higher stomatal density in cotton than in maize leaves (Figure S1a) provides more micron-sized stomatal pore entrance pathways for nanomaterials. Furthermore, stomatal guard cells in the epidermis appear to be more permeable and have a higher nanoparticle size limit than mesophyll cells containing chloroplasts (Figure 6a,c). Stomata guard cells have cell walls with mechanical properties that allow them to significantly enlarge or contract [94,116] and have an estimated pore size greater than 20 nm.[69] In contrast, leaf mesophyll cells do not undergo large changes in volume [94,116] and have smaller cell wall pore size[73]. These underlying structural and functional properties of plant cell walls may explain the high colocalization rates with nanoparticles in leaf guard cells (Figure 6). Together these leaf structural traits contribute to the differences in translocation of nanoparticles into leaf mesophyll cells and organelles and overall foliar delivery efficiencies.

Nanoparticle-leaf interaction models for designing nanoparticle charge and size

We built nanoparticle-leaf interaction (NLI) empirical models to identify and predict nanoparticle hydrodynamic size and zeta potential ranges that enable nanoparticle foliar topical

delivery with above average efficiencies into cotton and maize guard cells, extracellular space, and chloroplasts (Figure 6d and Table S2). NLI empirical models based on 95% confidence ellipse regions predict a 20 and 11 nm hydrodynamic size limit for efficient hydrophilic nanoparticle delivery into cotton and maize guard cells, respectively. These empirical models also highlight that nanoparticles with positive zeta potential and below this size limit can be efficiently delivered into chloroplasts and extracellular spaces of cotton leaves. Despite that FITC-SN18 nanoparticles have a below average delivery efficiency to guard cells in cotton (~35%), their nanoparticle size and charge overlapped with the 95% confidence ellipse region for efficient delivery. FITC-SN18 have silanol instead of carboxyl functional groups suggesting that nanoparticle surface chemical identity is an important factor that should be taken into account by NLI empirical models.

The hydrodynamic size limitation for hydrophilic nanoparticle delivery efficiency indicates that the plant cell wall pore size is an important barrier for nanoparticle translocation in plants, excluding hydrophilic nanoparticles depending on their size. Nanoparticles with amphiphilic coatings such as PVP have been reported to enable the delivery of nanomaterials (~50 nm)[103] larger than the size exclusion limits found in this study, highlighting the need of *n*-dimensional NLI models that include not only nanoparticle size and zeta potential, but also hydrophobicity, aspect ratio, core and surface chemistry. The PVP coated AuNPs penetrate through the hydrophobic cuticular domains of the leaf epidermis within 2 days. However, these AuNPs had a lower translocation efficiency through the leaf mesophyll, possibly due to the amphiphilic nature of PVP surface coating. Under the nanomaterial hydrodynamic size limit, positive charge is crucial for nanoparticles to have a high delivery efficiency into leaf cells and organelles. The different behavior between nanoparticles with positive and negative charge could be associated with the negatively charged cell walls in plants that act as ion exchange surfaces promoting the penetration of cationic nanoparticles but impeding the anionic ones.[75–77,117,118] High zeta potential of nanoparticles, independent of charge, has been reported to favor penetration through plant membranes according to studies and models based on isolated protoplasts and chloroplasts in which the plant cell wall is absent.[28,66] However, in leaf cotton cells the nanoparticles with the lowest zeta potential magnitude and hydrodynamic diameter (SA-CD2, -13.8 mV, 2 nm) were more efficiently delivered to chloroplasts than the other negatively charged nanoparticles. This

supports the idea that the size limiting effect of cell walls could be predominant *in vivo*, allowing the uptake of nanoparticles with smaller size. Understanding the physical and chemical interactions of nanoparticles with model and isolated cell walls may contribute to elucidate the underlying mechanisms of these chemical interactions.

Conclusions

We designed and synthesized nanoparticles, and developed high spatiotemporal resolution imaging tools for systematically assessing and modeling the role of charge and size on nanomaterial distribution in leaf cells. We studied rapid foliar delivery methods for nanoparticles in cotton and maize crops that could be translated to other plant species and field applications. We demonstrated that it is crucial to lower nanoparticle formulation surface tension (~22 mN/m) for rapid foliar delivery of hydrophilic nanoparticles with hydrodynamic size larger than 2 nm. Real time *in planta* confocal microscopy indicated that nanoparticles translocate across leaf surfaces through stomata and cuticular pathways. Overall, the efficient delivery of nanoparticles into guard cells, extracellular space, and chloroplasts is dependent on nanoparticle size and charge, and plant species. Our systematic assessment of nanoparticle charge and size effect on their leaf cellular distribution is represented in NLI empirical models acting as predicting tools of the behavior of similar hydrophilic nanoparticles in cotton and maize leaves. The hydrodynamic size limit for efficient nanoparticle delivery into leaf cells was determined at 20 and 11 nm for cotton and maize, respectively, which points out to possible different cell wall pore size for these two plant species. Positive nanoparticle charge results in higher foliar delivery efficiencies into chloroplasts, possibly due to their higher affinity with the negatively charged plant cell walls and negative transmembrane electrical potential of the cell membrane. Although cotton and maize have contrasting leaf anatomic characteristics of the dicotyledons and monocotyledons, respectively, we expect that other plant species within these large plant taxa would show variations in hydrodynamic size and zeta potential range for efficient delivery of nanoparticles to specific cells and organelles. This study provides a framework of tools and approaches to assess and model the interactions between nanoparticle properties (hydrodynamic size and zeta potential) and plant cells and organelles *in vivo*.

Understanding and modeling the role of nanoparticle charge, size, hydrophobicity and other chemical and physical properties on their interactions with leaf surfaces will enable a more efficient and controlled use of nanoscale agrochemicals. Few studies have addressed how nanoparticle translocation and distribution in plants is affected by shape and composition of nanomaterials. However, accumulation and transport of gold nanoparticles in plants has been reported to depend on their aspect ratio[50] and hydrophobicity.[103] Nanoparticle transformations including corona formation by proteins, lipids, or carbohydrates in different plant species should also be assessed to determine the nanoparticle stability, uptake and translocation in plant organs and cell compartments, as well as their toxicity to plants.[119–122] Both nanomaterial size and surface properties have been reported to play a key role in determining nanoparticle corona formation in non-plant biological fluids.[119] This in turn is expected to have an impact on nanoparticle translocation and distribution in plants. However, the formation of plant biochemical coronas on nanoparticles is poorly understood and has been addressed by only a handful of studies.[123,124]

Similar to the pharmacokinetics field in biomedical research,[125–130] the emergent research area of plant nanokinetics aims at modeling nanoparticle uptake dynamics and distribution in plants. Recent studies in this area are highlighting how nanoparticle properties (*e.g.* size, charge) impact their translocation and distribution in isolated chloroplasts,[28] protoplasts without cell walls,[66] and *in vivo* in plants as reported in this study. Comparisons between exposure studies at different timescales would allow the creation of plant nanokinetic models that merge spatial and temporal nanoparticle-leaf interaction components for determining and quantifying the dynamic behavior of nanoparticle uptake, translocation, distribution, and excretion in plant structures. Plant nanokinetic assessments can lead to effective and safe plant-nanotechnology management, enhancing the efficacy of nanoparticles on plant health while reducing exposure to humans and the environment.

Methods

Synthesis of nanoparticles

The CDs were synthesized by modifying a protocol reported by Khan *et al*.[131] Briefly, 2.40 g (40 mmol) of urea (99.2%, Fisher), 1.92 g (10 mmol) of citric acid (CA, 99.7%, Fisher), and 1.35 mL of ammonium hydroxide (NH_3•H_2O, 30~33%, Aldrich) was dissolved into 2 mL of molecular water (Corning). The mixture was kept in a 50 mL beaker in an oven at 180 ℃ for 1h and 20min. After cooled down to room temperature, the product was dissolved in 300 mL of molecular water, filtered with filter paper (Whatman, pore size, 11 μm), and the collected filtrate was denoted as CDs. To synthesize PEI-CD2 and PEI-CD6, the CDs were functionalized with PEI600 (branched polyethyleneimine, M.W. 600, 99%, Alfa Aesar) and PEI10k (branched polyethyleneimine, M.W. ~10k, 99%, Alfa Aesar), respectively. The CDs were suspended in molecular water to yield 4 mL of solution with a CD concentration of 5 mg/mL and the pH adjusted to 10 by adding NaOH solution (20 mg/mL). This solution was added slowly while stirring into a 0.8 mL of PEI600 or PEI10k solution (100 mg/mL). The mixture was kept stirring for 0.5h before being sealed in Falcon tubes and treated at 85 ℃ for 16h in the oven. The product was cooled down to room temperature, condensed and purified with a mixture of molecular water, ethanol (absolute, Fisher), and chloroform (99%, Fisher) by centrifugation at 4,500 rpm for 5 times. The resulting PEI-CD solution was collected and blown with air for 30 min to remove ethanol and chloroform residuals. The PEI-CDs were redissolved in molecular water. To synthesize SA-CD2 and SA-CD6, PEI-CD2 and PEI-CD6 were further treated with succinic anhydride (SA, 99%, Alfa Aesar). The PEI-CD2 or PEI-CD6 were diluted with molecular water to yield 1 mL of solution with a concentration of 5 mg/mL. Then this solution was diluted by adding 3 mL of DMF (*N,N*-dimethylformamide, >99%, Sigma), followed by adding 1 mL of SA solution (250 mg/mL) in DMF while stirring. The mixture was kept stirring for 3h before condensed and purified with a mixture of molecular water, ethanol, and chloroform by centrifugation at 4,500 rpm for 5 times. The resulting SA-CD solution was collected, and blown with air for 30 min to remove ethanol and chloroform residuals, and SA-CDs were redissolved in molecular water.

The PAA [poly(acrylic acid), M.W. ~1800, Sigma Aldrich] functionalized cerium oxide nanoparticles (PNC) were synthesized as in Wu *et al.*[24] with modifications to control negatively charged PNC size. For PNC2, 0.217 g of $Ce(NO_3)_3$•$6H_2O$ (cerium (III) nitric hexahydrate, 99%, Aldrich) in 0.5 mL of molecular water was mixed with 0.450 g of PAA in another 0.5 mL of

molecular water. The mixture was then added into 3 mL of NH_3•H_2O while vigorously stirring. For PNC11, 0.217 g of $Ce(NO_3)_3$•$6H_2O$ in 0.5 mL of molecular water was added rapidly into 3 mL of NH_3•H_2O while vigorously stirring. After 1 min, 0.450 g of PAA in 0.5 mL of molecular water was added to the mixture. For PNC16, 0.217 g of $Ce(NO_3)_3$• $6H_2O$ in 0.5 mL of molecular water was added slowly (60s) into 3 mL of NH_3•H_2O while vigorously stirring. After 1 min, 0.450 g of PAA in 0.5 mL of molecular water was added to the mixture. All the mixtures were kept stirring for 24 h before centrifugation to remove large aggregates, which was followed by purification with centrifugation filters (Amicon cell, MWCO 10k, Millipore Inc.) for 5 times at 4,500 rpm.

To synthesize positively charged aminated dextran functionalized cerium oxide nanoparticles (ADNCs), dextran functionalized cerium oxide nanoparticles (DNCs) were prepared by following protocols in Asati *et al.*[132] with modifications, followed by functionalization with DEAE in NaOH solution.[133] For DNC8, 0.217 g of $Ce(NO_3)_3$•$6H_2O$ in 0.5 mL of molecular water was mixed with 1.010 g dextran (M.W. ~6,000, Alfa Aesar) in 0.5 mL of molecular water. For DNC12, 0.217 g of $Ce(NO_3)_3$•$6H_2O$ in 0.5 mL DI water was mixed with 0.450 g dextran in 0.5 mL DI water. These solutions were separately added into 3 mL of NH_3•H_2O while vigorously stirring for 24 h. Centrifugation was used to remove large aggregates before purification with centrifugation filters (Amicon cell MWCO 10k, Millipore Inc.) for 5 times at 4,500 rpm. The purified DNC8 and DNC12 were redissolved in 10 mL of molecular water and mixed with 10 mL of NaOH solution (80 mg/mL). Then 2.40 g of DEAE•HCl (diethylaminoethyl hydrochloride, 99.5%, Acros) was added to the mixture while vigorously stirring. The mixtures were stirred overnight before purification to remove unreacted free reagents and side products by centrifugation using centrifugation filters (Amicon cell MWCO 10k, Millipore Inc.) to yield ADNC8 and ADNC12.

To label cerium oxide nanoparticles with DiI ((2Z)-2-[(E)-3- (3,3-dimethyl-1-octadecylindol-1-ium-2-yl) prop-2-enylidene] -3,3-dimethyl-1-octadecylindole perchlorate, Invitrogen), the hydrophobic fluorescent dye was encapsulated and stabilized in the polymer coating (PAA or dextran) in PNCs and ADNCs following Asati *et al*.[134] Briefly, 4 mL of PNCs or ADNCs aqueous solution (1.5 mg/mL) was added to 0.2 mL of DiI solution (0.3 mg/mL) in DMSO

(Dimethyl sulfoxide, 99.9%, Fisher) while stirring at 1,000 rpm. After incubation overnight, the mixture was purified by centrifugation at 4,500 rpm using Amicon cell (MWCO 10k, Millipore Inc.) for 5 times to remove free DiI molecules from DiI labeled PNC and ADNC.

The negatively charged silica nanoparticles labeled with FITC (fluorescein isothiocyanate, Isomer I, 90%, Acros) were synthesized following the protocol reported by Larson *et al*.[135] with modifications. Briefly, FITC-silane compound was synthesized by reacting 3.9 mg of FITC with 20 μL of APTMS ((3-Aminopropyl)triethoxysilane, >97%, Aldrich) and forming a covalent isothiourea linkage in 80 μL of ethanol and DMSO mixture (3:1, v/v). After half an hour, 10 μL of prepared FITC-saline compound solution was added into a solvent mixture with 9 mL of ethanol and 150 μL molecular water and stirred at 500 rpm in a 50 mL falcon tube, followed by the addition of 350 μL of TEOS (tetraethyl orthosilicate, 98%, Aldrich) and 100 μL of $NH_3 \bullet H_2O$ in order. The mixture was kept stirred overnight in the dark before purification to remove unreacted free reagents by centrifugation using centrifugal filters (Amicon cell MWCO 10k, Millipore Inc.) to yield FITC-SN18.

Nanoparticle characterization

UV-vis spectra of nanoparticles were collected in a micro quartz cuvette (10 mm × 2 mm, path length 10 mm) using a Shimadzu UV-2600 spectrometer. Fluorescence emission spectra of nanoparticle samples were acquired with a PTI QuantaMaster 400 fluorometer in a quartz cuvette (10 mm × 10 mm). Fourier-transform infrared (FTIR) spectroscopy was performed with a Nicolet 6700 FTIR spectrometer. The size of nanoparticles was characterized with both dynamic light scattering (DLS) and transmission electron microscopy (TEM). DLS measurements were conducted with a Malvern Zetasizer Nano S. TEM was performed on a Philips FEI Tecnai 12 microscope operated at an accelerating voltage of 120 kV. The TEM samples were prepared by placing one drop of particle solution onto a Cu grid (400 mesh, Ted Pella) followed by drying at laboratory conditions. Zeta potential was measured with a Malvern Zetasizer Nano ZS with nanoparticles (0.1 mg/mL) dispersed in NaCl buffer (0.1 mM) and analyzed by the Hückel approximation. For a 0.1 mM aqueous solution, the Debye length ($1/\kappa$) is ~ 30 nm. Thus, the Hückel approximation applies for all 10 types of nanoparticles in this study with size below 20 nm.[136–138] Because surfactant bubble formation interferes with DLS measurements, nanoparticle stability in surfactants was assessed by centrifugation. All

nanoparticles formulations were centrifuged at 13.2 k rpm for 15 min to determine potential aggregation, and no precipitates were observed for CDs, cerium oxide, and silica nanoparticles.

Plant growth

Cotton seeds (*Gossypium hirsutum* L.) cultivar Acala 1517-08 were sterilized for 15 min in 9% H_2O_2, washed three times followed by 24 h imbibition in double distilled water, and then planted in the plastic pots (10×10×9 cm^3) filled with standard soil mix (Sunshine, LC1 mix). Maize (*Zea mays* L., golden bantam) seeds were planted in the plastic pots (8.5×8.5×8.5 cm^3) using the same soil described above. Cotton and maize plants were grown in a LED growth chamber (HiPoint) at 21/26 ℃ (day/night) with a 14 h photoperiod at photosynthetic active radiation (PAR) of 360 to 450 and 200 to 250 μmol•m^{-2}•s^{-1}, respectively. Three-week-old cotton and 10-day-old maize seedlings were used in experiments for this study when plants were at the two true leaf stage.

Leaf characterization

All leaves used in this study were the first true leaves of cotton and maize plants at the two-leaf stage. Scanning electron microscopy (SEM) of the leaf epidermis was performed with a Hitachi TM-1000 (Japan). SEM samples of cotton and maize leaves were cut into 1 cm^2 and immersed in isopentane (cooled by liquid nitrogen) for 5 s before placing them onto the sample stage for imaging. The SEM images were analyzed with ImageJ to measure stomatal densities and lengths. Leaf cross-section images were visualized under a microscope (BZ-X710, Keyence, Osaka, Japan). Leaf cross-section samples of cotton and corn leaves were embedded by 7% agarose, sectioned into 40 and 50 μm under an oscillating tissue slicer (EMS 500, Electron Microscopy Sciences Inc., and Hatfield, PA). Samples were stained with 0.01% Toluidine Blue O for 1 min, and washed gently with distilled water.[139] The leaf autofluorescence spectra were acquired with a PTI QuantaMaster 400 fluorometer with cotton or maize leaf mounted on a solid sample holder. Leaf chlorophyll content was quantified with a SPAD 502 plus chlorophyll meter (Konica Minolta, Tokyo, Japan) and measured as chlorophyll content index (CCI).

Composition and application of foliar nanoparticle formulations

All nanoparticle formulations were composed of one surfactant (Silwet L-77, Bio World, 0.2 % applied for cotton or 0.3 % for maize, or Triton X-100, IBI Scientific, 0.2% for both cotton and maize) as a wetting agent. The surface tension of nanoparticle formulations was measured by the

Wilhelmy plate method using a surface tensiometer (Kino, Model A3). Briefly, the platinum plate was cleaned with DI water and heated with an alcohol burner until the plate turned red (~30s) before it was hung onto the hook of the surface tensiometer. Nanoparticle formulation (5 mL) was added into a clean glass sample container and placed on the surface tensiometer stage below but without touching the plate. After the tensiometer reading was stable, the sample stage was raised using a micrometer until the bottom of the plate is in contact with the surface of the formulation. At this point, the measured surface tension values from the tensiometer were recorded. We assessed if DiI and FITC fluorescent dyes dissociate from the nanoparticles in the presence of surfactants. The DiI-PNC2, DiI-ADNC12, and FITC-SN18 were suspended in Silwet L-77 formulations, and centrifuged at 4500 rpm for 30 min in Amicon cell centrifugal filters (MWCO 3k, Millipore Inc.). UV-vis spectrophotometry was used to detect potential absorbance peaks for DiI or FITC dyes. A humectant (glycerol, 3%) was also included in formulations to improve attachment and retention of the applied formulations on the maize leaf surface (Figure S22). The nanoparticle concentrations were selected based on optimization of fluorescence signal for imaging by confocal microscopy and maintenance of leaf health upon nanoparticle exposure. The concentrations of CDs were 0.5 and 5 mg/mL for cotton and maize, respectively. The concentration of the cerium oxide nanoparticles and silica nanoparticles were 0.5 mg/mL for both cotton and maize. Non-surfactant formulation controls containing CDs (PEI-CD2 and SA-CD2) at the same concentrations and volumes as those with surfactants were applied to cotton and maize leaves while mounted on a flat surface to prevent non-surfactant formulation from dripping off the leaf surface. Cotton and maize leaves were in the dark during application of nanoparticles onto the whole surface of the first true leaf.

Confocal microscopy imaging of nanoparticles in leaves

Leaves were imaged by using an inverted Leica TCS-SP5 spectral confocal laser scanning microscope from the leaf epidermis, where higher nanoparticle fluorescence signals were detected, and into the leaf mesophyll. Samples were mounted on microscope slides (Corning 2948-75X25) having a Carolina observation gel chamber (~1 mm in thickness) made with a cork borer (diameter, 8 mm). A leaf disk was taken from a treated leaf with a cork borer (diameter, 6 mm), immersed in the chamber filled with perfluorodecalin (PFD, 90%, Acros) and sealed with a coverslip (VWR). Leaf disks from non-surfactant formulation controls were taken right

underneath the site of application. Confocal microscopy imaging settings were as follows: 40× wet objective (HCX PL APO CS 40.0x1.10 WATER UV, Leica Microsystems, Germany); laser excitation 405 nm, 514 nm, and 476 nm for samples treated with CDs, NCs, and FITC-SN18, respectively; *z*-stack section thickness = 2 μm; line average = 4; PMT1 (NP channel), 410–490, 550–615, or 500–600 nm for samples treated with CDs, NCs, or FITC-SN18, respectively; PMT2 (chlorophyll channel), 700–790 nm. The x-y resolution based on the 40× objective numerical aperture (NA=1.1) and laser wavelengths 405, 476, and 514 nm was calculated at 225, 264, 285 nm, respectively, using the equation $d=0.61\lambda/NA$, where d is resolution and λ is the light wavelength. At least five cotton or maize plants were used for confocal microscopy imaging from the leaf epidermis into the mesophyll cells. Representative confocal microscopy images of nanoparticle treatments (Figure 5 and S16-S19), and control leaf samples exposed to surfactant alone are shown (Figure S23). Guard cell and NP colocalization was determined by analyzing confocal images as follows. The total number of guard cells were counted in the confocal microscopy images on the leaf epidermis, where all guard cells were outlined by the fluorescence of foliarly applied nanoparticles. Guard cells with nanoparticles inside were identified through confocal microscopy z-stacks from the leaf epidermis into the mesophyll. The colocalization rates were calculated as the percentage of guard cell pairs with nanoparticle fluorescence relative to total number of guard cell pairs. Colocalization of leaf extracellular space and NPs was determined in confocal images in which mesophyll cell boundaries were delineated by chloroplasts localized at the plant cell membrane due to exposure to laser excitation during confocal microscopy imaging.[111–113] Fluorescent dyes were not used to label plant cell boundaries because they quench CD fluorescence. Instead chloroplasts were used to delineate the plasma membrane boundary in leaf mesophyll cells upon laser excitation as reported previously.[111–113] This was confirmed in cotton and maize leaves by imaging chloroplasts in cells with cell membranes stained by FM 1-43 fluorescent dye (Figure S21). Cotton and maize leaves were infiltrated with FM 1-43 (10 μg/mL) in TES buffer (10 mM) to stain cell membranes[140–142] using a needleless syringe (1 mL) and incubated for 10 min. Leaf disks were taken for confocal microscopy imaging using 40× wet objective (HCX PL APO CS 40.0×1.10 WATER UV, Leica Microsystems, Germany); laser excitation 405, 476, or 514 nm, respectively; z-stack section thickness = 2 μm; line average = 4; PMT1 (FM1-43 channel), 520–620 nm; PMT2 (chlorophyll channel), 700–790 nm. All pixels inside the cells were removed

using ImageJ to obtain the extracellular space. The extracellular space and NP colocalization was calculated as the area occupied by NPs in the extracellular space divided by the whole area of extracellular space. Colocalization between NPs and chloroplasts was analyzed with LAS (Leica Application Suite) AF Lite software. Six line sections were drawn across the so-called "region of interest" (ROI) with 30 μm interval on the confocal images. The corresponding distribution profiles of fluorescence intensity of NPs and chloroplast autofluorescence for each ROI line were plotted. The colocalization rate of chloroplasts with NPs was counted as the proportion of chloroplast pigment fluorescence emission peaks which are overlapped with NP fluorescence peaks out of all chloroplast peaks. We only counted chloroplast emission peaks fully overlapped with NP emission peaks and excluded partially overlapped peaks to eliminate potential false positive colocalization due to the confocal imaging resolution limit. Nanoparticle overlay with chloroplast and guard cell edges within the x-y resolution was not considered as colocalization with these plant structures.

High spatial and temporal resolution confocal images of CDs entering cotton and maize leaves *in planta* were acquired with an upright Zeiss 880 confocal laser scanning microscope using a 40 × water dipping objective (LD LCI Plan-Apochromat 40×/1.2 Imm Corr DIC M27). Plants were taken out from pots carefully with the soil attached on their roots to avoid root damage. Immediately, the plant roots were covered with moist paper towels, plastic film, and foil. The first true leaves were mounted onto microscope slides and secured with double-sided tape. Coverslips were then placed over the leaves and mounted to microscope slides with super glue, so that a narrow space was left between the coverslip and the leaves for delivering the CD formulation. Formulations without CDs were applied first to record control z-stack images in flat scanning areas on the leaf surface where both leaf mesophyll cells and stomata were previously identified. Then a CD formulation was added and the z-stack images were taken continuously with section thickness of 2 μm and a scanning cycle about 2 to 5 mins depending on the z-stack layers. The formulation without nanoparticles was added every 15 min to keep the liquid layer in between the microscopy slide and the leaf lamina. Samples were excited with 405 nm (6.0%) and 458 nm (1.0%) laser lines, with an emission band recorded at 410-490 nm for CDs and 700-758 nm for chlorophyll autofluorescence. The x-y resolution based on the 40× objective (NA=1.2) and laser wavelengths 405 and 458 nm was calculated at 206 and 233 nm, respectively, using the

equation d=0.61λ/NA, where d is resolution and λ is the light wavelength. ImageJ was used to reconstruct 3D images and videos of CDs in leaves (Video S1-S8).

Statistical analysis

Statistical analysis was performed in SPSS 20.0 software (IBM, New York, USA). Zeta potential comparisons and nanoparticle colocalization differences in guard cells, extracellular space and chloroplasts were analyzed by nonparametric independent samples Kruskal-Wallis one-way ANOVA test. Calculation of efficient delivery regions based on confidence ellipse analysis[143,144] were possible only for plant cell compartments having three or more efficient combinations of nanoparticle size and charge. The ellipse parameters were calculated based on the hydrodynamic size and zeta potential of nanoparticles with above average delivery efficiency to guard cells, chloroplasts and extracellular space (Table S2). The ellipse center coordinates are means of hydrodynamic size and zeta potential, and ellipse axes lengths and rotation angle were calculated based on confidence levels and the covariance matrix of hydrodynamic size and zeta potential of nanoparticles (Table S2).

Supporting Information.

The Supporting Information is available free of charge on the ACS Publications website at DOI: xxxxxxx.

- **Figures S1 to S23.** Stomatal density and length of cotton and maize, leaf autofluorescence of cotton and maize, TEM images, FTIR and UV/vis spectra of nanoparticles, surface tension and pH values of nanoparticle formulations, representative confocal images for assessing leaf uptake of PEI-CD2 and SA-CD2 in cotton and maize leaves with Triton X-100 or Silwet L-77 as surfactant or in water formulation without surfactant, 3D renderings of confocal microscopy images showing nanoparticle delivery pathways from the leaf surface into mesophyll cells of cotton and maize, images of nanoparticle suspensions indicating high stability in surfactant formulation, UV-vis absorption spectra showing no fluorescent dye leaking from nanoparticles in the presence of Silwet L-77, leaf chlorophyll content patterns in cotton and maize after exposure to foliar topical

formulations (CDs) with Silwet L-77 as surfactants, high spatial and temporal resolution images of nanoparticle translocation pathways from the leaf surface into the mesophyll, confocal microscopy images with higher magnification of cotton and maize leaf mesophyll cells after foliar delivery of 10 types of nanoparticles suspended in formulation of Silwet L-77 as surfactant, positive linear correlation between colocalization rate of chloroplasts based on ROI analysis and Manders' overlap coefficient, representative confocal microscopy images of chloroplast autofluorescence and leaf mesophyll cells with FM 1-43 fluorescent dye, positive linear correlation between extracellular space area determined by chloroplast autofluorescence arrangement *versus* FM 1-43 labeled cell membranes, representative confocal images indicating colocalization of chloroplast autofluorescence with foliar-applied nanoparticles (PEI-CD6) using formulations with or without humectant (glycerol, 3%), representative confocal images showing no nanoparticle fluorescence when leaves were treated with control formulations without nanoparticles for cotton and maize.

- Table S1 and S2. Hydrodynamic size (average ± standard deviation, nm) and zeta potential (average ± standard deviation, mV) of nanoparticles, and confidence ellipse equation with corresponding parameters for determining nanoparticle efficient delivery regions.
- Video S1 to S16. Time-lapse videos showing uptake of CDs by cotton and maize leaves *in planta*, videos of reconstructed 3D confocal images of CD distribution in cotton and maize leaf tissues.

ORCID

Peiguang Hu: 0000-0002-9526-6295

Juan Pablo Giraldo: 0000-0002-8400-8944

Author Contributions

P.H. and J.A. contributed equally. J.P.G., P.H., and J.A. conceived and designed this study. P.H., J.A., and M.F. performed experiments. P.H., J.A., J.P.G., and H.W. analyzed the results. J.P.G.,

P.H., J.A., H.W., X.T., and Z.L. wrote the manuscript. All authors have read and agreed with the manuscript.

Current Address

[†]College of Plant Science & Technology, Huazhong Agricultural University, Wuhan 430070, China

Conflict of Interest

The authors declare no competing financial interests.

Acknowledgments

This work was supported by the National Science Foundation under the Center for Sustainable Nanotechnology, CHE-1503408. The CSN is part of the Centers for Chemical Innovation Program. Transmission Electron microscopy was performed on a TEM FEI Tecnai 12 in Central Facility for Advanced Microscopy and Microanalysis (CFAMM) at UC Riverside. Cotton seeds Acala 1517-08 were provided by Prof. Jinfa Zhang from the Department of Plant and Environmental Sciences, New Mexico State University. Jing An acknowledges funds from a Chinese Scholarship Council Fellowship.

Figure Legends

Figure 1. Nanoparticle translocation pathways and distribution in plant leaves with different anatomical properties. a, Nanoparticles (*e.g.* CDs, CeO_2 and SiO_2) translocate across the leaf epidermal barrier either through stomatal (red line) and/or cuticular (pink line) pathways, then move through the extracellular space and in between cell walls (apoplastic pathway) and/or enter the leaf mesophyll cells and translocate between cells through the cytosol (symplastic pathway). The translocation pathways are influenced by the differences in anatomical properties between dicot (cotton) and monocot (maize) plant leaves. Nanoparticles can localize in leaf cells

in the epidermis (*e.g.* guard cells), extracellular space, or organelles (*e.g.* chloroplasts). **b,** Representative SEM images of cotton and maize leaf epidermal surfaces indicating differences in stomatal arrangement, density, and length. **c,** Brightfield images of leaf cross-sections highlighting the differences in anatomy of leaf epidermal and mesophyll tissues in dicot (cotton) and monocot (maize) plant species. Arrows point to guard cells (red), extracellular space (cyan), and chloroplast (green).

Figure 2. Design and characterization of nanoparticle chemical and physical properties for understanding their interactions with leaf cell and organelles. **a,** Carbon dots (PEI-CDs and SA-CDs), CeO_2 (DiI-PNCs and DiI-ADNCs), and SiO_2 (FITC-SN) nanoparticles were synthesized with hydrodynamic diameters, measured by DLS, from 1.7-18 nm. **b,** Surface chemical modifications were used to generate hydrophilic nanoparticles with highly positive or negative zeta potential for understanding the role of charge in determining translocation through plant surfaces including the leaf cell walls, cell and organelle lipid bilayers, Mean ± SD. Zeta potential comparisons were analyzed by Kruskal-Wallis one-way ANOVA tests. Different lowercase letters indicate significant differences ($P < 0.05$). **c,** Nanoparticle optical properties were designed to optimize the fluorescence signal in the visible window within the range of low leaf background fluorescence emission for cotton and maize. Excitation wavelengths: 405 nm for leaves, PEI-CDs and SA-CDs; 514 nm for DiI-PNCs and DiI-ADNCs; and 476 nm for FITC-SN18. PEI-CDs, branched polyethyleneimine coated carbon dots; SA-CDs, succinic anhydride modified PEI-CDs; DiI-PNCs, poly(acrylic acid) coated cerium oxide nanoparticles labeled with DiI as fluorescent dye; DiI-ADNCs, aminated dextran coated cerium oxide nanoparticles labeled with DiI as fluorescent dye; FITC-SN18, silica nanoparticles labeled with FITC as fluorescent dye. Last digits in nanoparticle labels indicate hydrodynamic size, for example, PEI-CD2 (PEI-CD with hydrodynamic size about 2 nm).

Figure 3. Formulations with low surface tension enable nanoparticle foliar delivery into plant leaves. a, Comparison of foliar delivery of CDs suspended in formulations with low *versus* high surface tension using the surfactants Silwet L-77 (~22 mN/m) and Triton X-100 (~30 mN/m), respectively. Positively and negatively CDs of different sizes (PEI-CD2 (1.7 nm), SA-CD2 (1.9 nm), PEI-CD6 (5.5 nm), and SA-CD6 (6.4 nm)) were imaged by confocal microscopy to determine nanoparticle leaf uptake, n=5. **b,** Representative confocal fluorescence microscopy

images (2 μm z-axis, and 225 - 285 nm x-y resolution, Leica SP5) of the leaf mesophyll (cotton and maize) indicating leaf translocation of CDs larger than 5 nm (PEI-CD6 (5.5 nm), SA-CD6 (6.4 nm)) when nanoparticles are delivered in Silwet L-77. However, no CDs above 5 nm were observed inside leaves when the nanoparticles were delivered with Triton X-100. n=5, Mean ± SD. Images were collected after 3h incubation with nanoparticles. NP and Chl represent nanoparticles (green) and chloroplasts (magenta), respectively. The (+) and (-) indicate positively and negatively charged nanoparticles, respectively.

Figure 4. High spatial and temporal resolution imaging of nanoparticle translocation pathways from the leaf surface into the mesophyll *in planta*. Snapshots from confocal fluorescence microscopy videos showing pathways of CD movement (2 nm in size, green) in real-time (3.5 and 1.7 min resolution for cotton and maize, respectively) from the leaf surface into mesophyll cells and chloroplasts (magenta) (Video S1 and S2). In cotton, the CDs move through both cuticular and stomatal pathways through the leaf epidermis, whereas in maize the CDs penetrate the leaf surface mainly through the stomatal pathway. In both species, CDs delivered in Silwet L-77 move rapidly from the leaf epidermis into the mesophyll within 10-20 min. Arrows point to the stomatal pathways (white), and cuticular pathways (yellow). t=0 min represents images captured before nanoparticle formulation was added. 2 μm z-axis resolution, 206 - 233 nm x-y resolution (Zeiss 880).

Figure 5. Nanoparticle distribution in leaf cells and organelles. a, Representative confocal fluorescence microscopy images of foliar-delivered nanoparticles (green) to different tissue and cell compartments in cotton and maize leaves including chloroplasts (white arrows), extracellular space (cyan arrows), and stomatal guard cells (yellow arrows). Orthogonal views of representative confocal microscopy z-stacks displaying the colocalization of nanoparticles in **b,** chloroplasts with corresponding line transect colocalization analysis of nanoparticle and chloroplast fluorescence peak overlap, **c,** extracellular space, and **d,** stomatal guard cells (red arrow) and stomatal pores (orange arrow). 2 μm z-axis resolution, 225 - 285 nm x-y resolution (Leica SP5). Images were collected after 3h incubation with nanoparticles. NP and Chl represent nanoparticles (green) and chloroplasts (magenta), respectively. The (+) and (-) indicate positively and negatively charged nanoparticles, respectively.

Figure 6. Nanoparticle-Leaf interaction (NLI) empirical models for designing nanoparticle charge and size with improved delivery efficiency to specific leaf cells and organelles. Box plots of colocalization rates for positively and negatively charged nanoparticles ranging from 1.7-18 nm in size with **a,** guard cells in the leaf epidermis, **b,** extracellular space, and **c,** chloroplasts in the leaf mesophyll of cotton (left column) and maize (right column). Boxes represent the interquartile range from the first to the third quartile with squares as the medians; minimum and maximum values (snapped to mean − 1 × SD and mean + 1 × SD, SD = standard deviation) are shown with whiskers; red or blue circles are actual data points. Dotted lines represent the averages (grey) and standard errors (SE, black) of all non-zero data points. Nanoparticles with efficient delivery to guard cells, extracellular space, or chloroplasts are those with colocalization rates in the region above these averages minus SE (lower dotted black line). Nanoparticle colocalization differences in guard cells, extracellular space and chloroplasts were analyzed by Kruskal-Wallis one-way ANOVA. Different lowercase letters indicate significant differences ($P < 0.05$). **d,** NLI empirical models represented by 95% (dashed lines) and 90% (dash-dotted lines) confidence ellipses, indicating the size and zeta potential regions with predicted above average nanoparticle delivery efficiency to leaf guard cells, chloroplasts, and extracellular space.

References

(1) Alexandratos, N.; Bruinsma, J. World Agriculture towards 2030/2050: The 2012 Revision, 2012. Food and Agriculture Organization of the United Nations. http://www.fao.org/3/a-ap106e.pdf (accessed May 17, 2019)

(2) The Future of Food and Agriculture: Trends and Challenges, 2018. Food and Agriculture Organization of the United Nations. http://www.fao.org/3/a-i6583e.pdf (accessed May. 9, 2019)

(3) White, J. C.; Gardea-Torresdey, J. Achieving Food Security through the Very Small. *Nat. Nanotechnol.* **2018**, *13*, 627–629.

(4) Ray, D. K.; Mueller, N. D.; West, P. C.; Foley, J. A. Yield Trends Are Insufficient to Double Global Crop Production by 2050. *PLoS One* **2013**, DOI.org/10.1371/journal.pone.0066428.

(5) Kah, M.; Tufenkji, N.; White, J. C. Nano-Enabled Strategies to Enhance Crop Nutrition and Protection. *Nat. Nanotechnol.* **2019**, *14*, 532–540.

(6) Climate Impacts on Agriculture and Food Supply, 2016. The United States Environmental Protection Agency. https://19january2017snapshot.epa.gov/climate-impacts/climate-impacts-agriculture-and-food-supply_.html (accessed May 9, 2019).

(7) Schlenker, W.; Lobell, D. B. Robust Negative Impacts of Climate Change on African Agriculture. *Environ. Res. Lett.* **2010**, *5*, 014010.

(8) Piao, S.; Ciais, P.; Huang, Y.; Shen, Z.; Peng, S.; Li, J.; Zhou, L.; Liu, H.; Ma, Y.; Ding, Y.; Friedlingstein, P.; Liu, C.; Tan, K.; Yu, Y.; Zhang, T.; Fang, J. The Impacts of Climate Change on Water Resources and Agriculture in China. *Nature* **2010**, *467*, 43–51.
(9) Ladha, J. K.; Pathak, H.; J. Krupnik, T.; Six, J.; van Kessel, C. Efficiency of Fertilizer Nitrogen in Cereal Production: Retrospects and Prospects *Adv. Agron.* **2005**, *87*, 85–156
(10) van de Wiel, C. C. M.; van der Linden, C. G.; Scholten, O. E. Improving Phosphorus Use Efficiency in Agriculture: Opportunities for Breeding. *Euphytica* **2016**, *207*, 1–22.
(11) Syers, K.; Johnston, E.; Curtin, D. A New Perspective on the Efficiency of Phosphorus Fertilizer Use. *19th World Congress of Soil Science, Soil Solutions for a Changing World*; Brisbane, Australia; August 1–6, 2010; pp 1–3.
(12) Aktar, M. W.; Sengupta, D.; Chowdhury, A. Impact of Pesticides Use in Agriculture: Their Benefits and Hazards. *Interdiscip. Toxicol.* **2009**, *2*, 1–12.
(13) Mahvi, A. H.; Nouri, J.; Babaei, A. A.; Nabizadeh, R. Agricultural Activities Impact on Groundwater Nitrate Pollution. *Int. J. Environ. Sci. Tech.* **2005**, *2*, 41–47.
(14) Wimalawansa, S. A.; Wimalawansa, S. J. Agrochemical-Related Environmental Pollution: Effects on Human Health. *Global J. Biol. Agric. Health Sci.* **2014**, *3*, 72–83.
(15) Md. Muhibbullah; Salma Momotaz; A.T. Chowdhury. Use of Agrochemical Fertilizers and Their Impact on Soil, Water and Human Health in the Khamargao Village of Mymensingh District, Bangladesh. *J. Agron.* **2005**, *4*, 109–115.
(16) Duhan, J. S.; Kumar, R.; Kumar, N.; Kaur, P.; Nehra, K.; Duhan, S. Nanotechnology: The New Perspective in Precision Agriculture. *Biotechnol Rep (Amst)* **2017**, *15*, 11–23.
(17) Raliya, R.; Saharan, V.; Dimkpa, C.; Biswas, P. Nanofertilizer for Precision and Sustainable Agriculture: Current State and Future Perspectives. *J. Agric. Food Chem.* **2018**, *66*, 6487–6503.
(18) Chen, H.; Yada, R. Nanotechnologies in Agriculture: New Tools for Sustainable Development. *Trends Food Sci. Technol.* **2011**, *22*, 585–594.
(19) Marchiol, L. Nanotechnology in Agriculture: New Opportunities and Perspectives. In *New Visions in Plant Science*; Çelik, Ö., Ed.; InTech: London, 2018; pp 121–142.
(20) Sangeetha, J.; Thangadurai, D.; Hospet, R.; Purushotham, P.; Karekalammanavar, G.; Mundaragi, A. C.; David, M.; Shinge, M. R.; Thimmappa, S. C.; Prasad, R.; Harish, E. R. Agricultural Nanotechnology: Concepts, Benefits, and Risks. In *Nanotechnology: An Agricultural Paradigm*; Prasad, R., Kumar, M., Kumar, V., Eds.; Springer Singapore: Singapore, 2017; pp 1–17.
(21) Kaushal, M.; Wani, S. P. Nanosensors: Frontiers in Precision Agriculture. In *Nanotechnology: An Agricultural Paradigm*; Prasad, R., Kumar, M., Kumar, V., Eds.; Springer Singapore: Singapore, 2017; pp 279–291.
(22) Wu, H.; Shabala, L.; Shabala, S.; Giraldo, J. P. Hydroxyl Radical Scavenging by Cerium Oxide Nanoparticles Improves *Arabidopsis* Salinity Tolerance by Enhancing Leaf Mesophyll Potassium Retention. *Environ. Sci.: Nano* **2018**, *5*, 1567–1583.
(23) Djanaguiraman, M.; Nair, R.; Giraldo, J. P.; Prasad, P. V. V. Cerium Oxide Nanoparticles Decrease Drought-Induced Oxidative Damage in Sorghum Leading to Higher Photosynthesis and Grain Yield. *ACS Omega* **2018**, *3*, 14406–14416.
(24) Wu, H.; Tito, N.; Giraldo, J. P. Anionic Cerium Oxide Nanoparticles Protect Plant Photosynthesis from Abiotic Stress by Scavenging Reactive Oxygen Species. *ACS Nano* **2017**, *11*, 11283–11297.
(25) Lawrence, J. R.; Swerhone, G. D. W.; Dynes, J. J.; Hitchcock, A. P.; Korber, D. R. Complex Organic Corona Formation on Carbon Nanotubes Reduces Microbial Toxicity by Suppressing Reactive Oxygen Species Production. *Environ. Sci.: Nano* **2016**, *3*, 181–189.
(26) Tourinho, P. S.; Van Gestel, C. A. M.; Lofts, S.; Svendsen, C.; Soares, A. M.; Loureiro, S. Metal-Based Nanoparticles in Soil: Fate, Behavior, and Effects on Soil Invertebrates. *Environ. Toxicol. Chem.* **2012**, *31*, 1679–1692.
(27) Ma, J. F. Role of Silicon in Enhancing the Resistance of Plants to Biotic and Abiotic Stresses. *Soil Sci. Plant Nutr.* **2004**, *50*, 11–18.
(28) Wong, M. H.; Misra, R. P.; Giraldo, J. P.; Kwak, S.-Y.; Son, Y.; Landry, M. P.; Swan, J. W.;

Blankschtein, D.; Strano, M. S. Lipid Exchange Envelope Penetration (LEEP) of Nanoparticles for Plant Engineering: A Universal Localization Mechanism. *Nano Lett.* **2016**, *16*, 1161–1172.
(29) Giroto, A. S.; Guimarães, G. G. F.; Foschini, M.; Ribeiro, C. Role of Slow-Release Nanocomposite Fertilizers on Nitrogen and Phosphate Availability in Soil. *Sci. Rep.* **2017**, *7*, 46032.
(30) El-Aila, H. I.; El-Sayed, S. A. A.; Yassen, A. A. Response of Spinach Plants to Nanoparticles Fertilizer and Foliar Application of Iron. *Int. J. Environ* **2015**, *4*, 181–185.
(31) Singh, A.; Bhati, A.; Tripathi, K. M.; Sonkar, S. K. Nanocarbons in Agricultural Plants: Can Be a Potential Nanofertilizer? In *Nanotechnology in Environmental Science*; Hussain, C. M., Mishra, A. K., Eds; Wiley-VCH: Weinheim, Germany, 2018; pp 153–190.
(32) Kah, M. Nanopesticides and Nanofertilizers: Emerging Contaminants or Opportunities for Risk Mitigation? *Front Chem* **2015**, *3*, 64.
(33) Li, J.; Wu, H.; Santana, I.; Fahlgren, M.; Giraldo, J. P. Standoff Optical Glucose Sensing in Photosynthetic Organisms by a Quantum Dot Fluorescent Probe. *ACS Appl. Mater. Interfaces* **2018**, *10*, 28279–28289.
(34) Giraldo, J. P.; Landry, M. P.; Faltermeier, S. M.; McNicholas, T. P.; Iverson, N. M.; Boghossian, A. A.; Reuel, N. F.; Hilmer, A. J.; Sen, F.; Brew, J. A.; Strano, M. S. Plant Nanobionics Approach to Augment Photosynthesis and Biochemical Sensing. *Nat. Mater.* **2014**, *13*, 400–408.
(35) Giraldo, J. P.; Landry, M. P.; Kwak, S.-Y.; Jain, R. M.; Wong, M. H.; Iverson, N. M.; Ben-Naim, M.; Strano, M. S. A Ratiometric Sensor Using Single Chirality Near-Infrared Fluorescent Carbon Nanotubes: Application to *In Vivo* Monitoring. *Small* **2015**, *11*, 3973–3984.
(36) Wong, M. H.; Giraldo, J. P.; Kwak, S.-Y.; Koman, V. B.; Sinclair, R.; Lew, T. T. S.; Bisker, G.; Liu, P.; Strano, M. S. Nitroaromatic Detection and Infrared Communication from Wild-Type Plants Using Plant Nanobionics. *Nat. Mater.* **2017**, *16*, 264–272.
(37) Koman, V. B.; Lew, T. T. S.; Wong, M. H.; Kwak, S.-Y.; Giraldo, J. P.; Strano, M. S. Persistent Drought Monitoring Using a Microfluidic-Printed Electro-Mechanical Sensor of Stomata in Planta. *Lab Chip*, **2017**, *17* 4015–4024.
(38) Kwak, S.-Y.; Lew, T. T. S.; Sweeney, C. J.; Koman, V. B.; Wong, M. H.; Bohmert-Tatarev, K.; Snell, K. D.; Seo, J. S.; Chua, N.-H.; Strano, M. S. Chloroplast-Selective Gene Delivery and Expression in Planta Using Chitosan-Complexed Single-Walled Carbon Nanotube Carriers. *Nat. Nanotechnol.* **2019**, *14*, 447–455.
(39) Demirer, G. S.; Zhang, H.; Matos, J. L.; Goh, N. S.; Cunningham, F. J.; Sung, Y.; Chang, R.; Aditham, A. J.; Chio, L.; Cho, M.-J.; Staskawicz, B.; Landry, M. P. High Aspect Ratio Nanomaterials Enable Delivery of Functional Genetic Material without DNA Integration in Mature Plants. *Nat. Nanotechnol.* **2019**, *14*, 456–464.
(40) Le, V. N.; Rui, Y.; Gui, X.; Li, X.; Liu, S.; Han, Y. Uptake, Transport, Distribution and Bio-Effects of SiO_2 Nanoparticles in Bt-Transgenic Cotton. *J. Nanobiotechnology* **2014**, *12*, 50.
(41) Gogos, A.; Moll, J.; Klingenfuss, F.; van der Heijden, M.; Irin, F.; Green, M. J.; Zenobi, R.; Bucheli, T. D. Vertical Transport and Plant Uptake of Nanoparticles in a Soil Mesocosm Experiment. *J. Nanobiotechnology* **2016**, *14*, 40.
(42) Elmer, W. H.; White, J. C. The Use of Metallic Oxide Nanoparticles to Enhance Growth of Tomatoes and Eggplants in Disease Infested Soil or Soilless Medium. *Environ. Sci.: Nano,* **2016**, *3*, 1072–1079.
(43) Sharma, P.; Sharma, A.; Sharma, M.; Bhalla, N.; Estrela, P.; Jain, A.; Thakur, P.; Thakur, A. Nanomaterial Fungicides: *In Vitro* and *In Vivo* Antimycotic Activity of Cobalt and Nickel Nanoferrites on Phytopathogenic Fungi. *Global Challenges*. **2017**, *1*, 1770071.
(44) Kim, J.-H.; Oh, Y.; Yoon, H.; Hwang, I.; Chang, Y.-S. Iron Nanoparticle-Induced Activation of Plasma Membrane H^+-ATPase Promotes Stomatal Opening in *Arabidopsis thaliana*. *Environ. Sci. Technol.* **2015**, *49*, 1113–1119.
(45) Wu, H.; Santana, I.; Dansie, J.; Giraldo, J. P. *In Vivo* Delivery of Nanoparticles into Plant Leaves. *Curr. Protoc. Chem. Biol.* **2017**, *9*, 269–284.
(46) Brillault, L.; Jutras, P. V.; Dashti, N.; Thuenemann, E. C.; Morgan, G.; Lomonossoff, G. P.;

Landsberg, M. J.; Sainsbury, F. Engineering Recombinant Virus-Like Nanoparticles from Plants for Cellular Delivery. *ACS Nano* **2017**, *11*, 3476–3484.
(47) Makhotenko, A. V.; Snigir, E. A.; Kalinina, N. O.; Makarov, V. V.; Taliansky, M. E. Data on a Delivery of Biomolecules into *Nicotiana benthamiana* Leaves Using Different Nanoparticles. *Data Brief* **2018**, *16*, 1034–1037.
(48) Huang, X.; Stein, B. D.; Cheng, H.; Malyutin, A.; Tsvetkova, I. B.; Baxter, D. V.; Remmes, N. B.; Verchot, J.; Kao, C.; Bronstein, L. M.; Dragnea, B. Magnetic Virus-Like Nanoparticles in *N. benthamiana* Plants: A New Paradigm for Environmental and Agronomic Biotechnological Research. *ACS Nano* **2011**, *5*, 4037–4045.
(49) Lv, J.; Christie, P.; Zhang, S. Uptake, Translocation, and Transformation of Metal-Based Nanoparticles in Plants: Recent Advances and Methodological Challenges. *Environ. Sci.: Nano* **2019**, *6*, 41–59.
(50) Raliya, R.; Franke, C.; Chavalmane, S.; Nair, R.; Reed, N.; Biswas, P. Quantitative Understanding of Nanoparticle Uptake in Watermelon Plants. *Front. Plant Sci.* **2016**, *7*, 1288.
(51) Karny, A.; Zinger, A.; Kajal, A.; Shainsky-Roitman, J.; Schroeder, A. Therapeutic Nanoparticles Penetrate Leaves and Deliver Nutrients to Agricultural Crops. *Sci. Rep.* **2018**, *8*, 7589.
(52) Wang, W.-N.; Tarafdar, J. C.; Biswas, P. Nanoparticle Synthesis and Delivery by an Aerosol Route for Watermelon Plant Foliar Uptake. *J. Nanopart. Res.* **2013**, *15*, 1417.
(53) Kranjc, E.; Mazej, D.; Regvar, M.; Drobne, D.; Remškar, M. Foliar Surface Free Energy Affects Platinum Nanoparticle Adhesion, Uptake, and Translocation from Leaves to Roots in Arugula and Escarole. *Environ. Sci.: Nano* **2018**, *5*, 520–532.
(54) Etxeberria, E.; Gonzalez, P.; Bhattacharya, P.; Sharma, P.; Ke, P. C. Determining the Size Exclusion for Nanoparticles in Citrus Leaves. *HortScience* **2016**, *51*, 732–737.
(55) Zhao, L.; Ortiz, C.; Adeleye, A. S.; Hu, Q.; Zhou, H.; Huang, Y.; Keller, A. A. Metabolomics to Detect Response of Lettuce (*Lactuca sativa*) to $Cu(OH)_2$ Nanopesticides: Oxidative Stress Response and Detoxification Mechanisms. *Environ. Sci. Technol.* **2016**, *50*, 9697–9707.
(56) Hong, J.; Peralta-Videa, J. R.; Rico, C.; Sahi, S.; Viveros, M. N.; Bartonjo, J.; Zhao, L.; Gardea-Torresdey, J. L. Evidence of Translocation and Physiological Impacts of Foliar Applied CeO_2 Nanoparticles on Cucumber (*Cucumis sativus*) Plants. *Environ. Sci. Technol.* **2014**, *48*, 4376–4385.
(57) Keller, A. A.; Huang, Y.; Nelson, J. Detection of Nanoparticles in Edible Plant Tissues Exposed to Nano-Copper Using Single-Particle ICP-MS. *J. Nanopart. Res.* **2018**, *20*, 101.
(58) Larue, C.; Castillo-Michel, H.; Sobanska, S.; Cécillon, L.; Bureau, S.; Barthès, V.; Ouerdane, L.; Carrière, M.; Sarret, G. Foliar Exposure of the Crop *Lactuca sativa* to Silver Nanoparticles: Evidence for Internalization and Changes in Ag Speciation. *J. Hazard. Mater.* **2014**, *264*, 98–106.
(59) Corredor, E.; Testillano, P. S.; Coronado, M.-J.; González-Melendi, P.; Fernández-Pacheco, R.; Marquina, C.; Ibarra, M. R.; de la Fuente, J. M.; Rubiales, D.; Pérez-de-Luque, A.; Risueño, M.-C. Nanoparticle Penetration and Transport in Living Pumpkin Plants: *In Situ* Subcellular Identification. *BMC Plant Biol.* **2009**, *9*, 45.
(60) Li, H.; Huang, J.; Lu, F.; Liu, Y.; Song, Y.; Sun, Y.; Zhong, J.; Huang, H.; Wang, Y.; Li, S.; Lifshitz, Y.; Lee, S.-T.; Kang, Z. Impacts of Carbon Dots on Rice Plants: Boosting the Growth and Improving the Disease Resistance. *ACS Appl. Bio Mater.* **2018**, *1*, 663–672.
(61) Ma, C.; White, J. C.; Zhao, J.; Zhao, Q.; Xing, B. Uptake of Engineered Nanoparticles by Food Crops: Characterization, Mechanisms, and Implications. *Annu. Rev. Food Sci. Technol.* **2018**, *9*, 129–153.
(62) Rodrigues, S. M.; Trindade, T.; Duarte, A. C.; Pereira, E.; Koopmans, G. F.; Römkens, P. F. A. M. A Framework to Measure the Availability of Engineered Nanoparticles in Soils: Trends in Soil Tests and Analytical Tools. *Trends Analyt. Chem.* **2016**, *75*, 129–140.
(63) Spielman-Sun, E.; Lombi, E.; Donner, E.; Howard, D.; Unrine, J. M.; Lowry, G. V. Impact of Surface Charge on Cerium Oxide Nanoparticle Uptake and Translocation by Wheat (*Triticum aestivum*). *Environ. Sci. Technol.* **2017**, *51*, 7361–7368.
(64) Li, J.; Tappero, R. V.; Acerbo, A. S.; Yan, H.; Chu, Y.; Lowry, G. V.; Unrine, J. M. Effect of CeO_2

Nanomaterial Surface Functional Groups on Tissue and Subcellular Distribution of Ce in Tomato (*Solanum lycopersicum*). *Environ. Sci.: Nano* **2019**, *6*, 273–285.
(65) Avellan, A.; Schwab, F.; Masion, A.; Chaurand, P.; Borschneck, D.; Vidal, V.; Rose, J.; Santaella, C.; Levard, C. Nanoparticle Uptake in Plants: Gold Nanomaterial Localized in Roots of *Arabidopsis thaliana* by X-Ray Computed Nanotomography and Hyperspectral Imaging. *Environ. Sci. Technol.* **2017**, *51*, 8682–8691.
(66) Lew, T. T. S.; Wong, M. H.; Kwak, S.-Y.; Sinclair, R.; Koman, V. B.; Strano, M. S. Rational Design Principles for the Transport and Subcellular Distribution of Nanomaterials into Plant Protoplasts. *Small* **2018**, *14*, 1802086.
(67) Schönherr, J. Characterization of Aqueous Pores in Plant Cuticles and Permeation of Ionic Solutes. *J. Exp. Bot.* **2006**, *57*, 2471–2491.
(68) Kerstiens, G. Water Transport in Plant Cuticles: An Update. *J. Exp. Bot.* **2006**, *57*, 2493–2499.
(69) Eichert, T.; Goldbach, H. E. Equivalent Pore Radii of Hydrophilic Foliar Uptake Routes in Stomatous and Astomatous Leaf Surfaces – Further Evidence for a Stomatal Pathway. *Physiol. Plant.* **2008**, *132*, 491–502.
(70) Popp, C.; Burghardt, M.; Friedmann, A.; Riederer, M. Characterization of Hydrophilic and Lipophilic Pathways of Hedera Helix L. Cuticular Membranes: Permeation of Water and Uncharged Organic Compounds. *J. Exp. Bot.* **2005**, *56*, 2797–2806.
(71) Eichert, T.; Kurtz, A.; Steiner, U.; Goldbach, H. E. Size Exclusion Limits and Lateral Heterogeneity of the Stomatal Foliar Uptake Pathway for Aqueous Solutes and Water-Suspended Nanoparticles. *Physiol. Plant.* **2008**, *134*, 151–160.
(72) Zeng, Y.; Himmel, M. E.; Ding, S.-Y. Visualizing Chemical Functionality in Plant Cell Walls. *Biotechnol. Biofuels* **2017**, *10*, 263.
(73) Albersheim, P.; Darvill, A.; Roberts, K.; Sederoff, R.; Staehelin, A. *Plant Cell Walls: From Chemistry to Biology*; Garland Science: New York, 2010; pp 241–242.
(74) Starrach, N.; Mayer, W.-E. Unequal Distribution of Fixed Negative Charges in Isolated Cell Walls of Various Tissues in Primary Leaves of Phaseolus. *J. Plant Physiol.* **1986**, *126*, 213–222.
(75) Fritz, E. Measurement of Cation Exchange Capacity (CEC) of Plant Cell Walls by X-Ray Microanalysis (EDX) in the Transmission Electron Microscope. *Microsc. Microanal.* **2007**, *13*, 233–244.
(76) Meychik, N. R.; Yermakov, I. P. Ion Exchange Properties of Plant Root Cell Walls. *Plant Soil* **2001**, *234*, 181–193.
(77) Szatanik-Kloc, A.; Szerement, J.; Józefaciuk, G. The Role of Cell Walls and Pectins in Cation Exchange and Surface Area of Plant Roots. *J. Plant Physiol.* **2017**, *215*, 85–90.
(78) Li, X.; Rui, M.; Song, J.; Shen, Z.; Zeng, H. Carbon and Graphene Quantum Dots for Optoelectronic and Energy Devices: A Review. *Adv. Funct. Mater.* **2015**, *25*, 4929–4947.
(79) Lim, S. Y.; Shen, W.; Gao, Z. Carbon Quantum Dots and Their Applications. *Chem. Soc. Rev.* **2015**, *44*, 362–381.
(80) Wang, R.; Lu, K.-Q.; Tang, Z.-R.; Xu, Y.-J. Recent Progress in Carbon Quantum Dots: Synthesis, Properties and Applications in Photocatalysis. *J. Mater. Chem. A Mater. Energy Sustain.* **2017**, *5*, 3717–3734.
(81) Das, R.; Bandyopadhyay, R.; Pramanik, P. Carbon Quantum Dots from Natural Resource: A Review. *Mater. Today Chem.* **2018**, *8*, 96–109.
(82) Yang, S.-T.; Cao, L.; Luo, P. G.; Lu, F.; Wang, X.; Wang, H.; Meziani, M. J.; Liu, Y.; Qi, G.; Sun, Y.-P. Carbon Dots for Optical Imaging *In Vivo*. *J. Am. Chem. Soc.* **2009**, *131*, 11308–11309.
(83) Cao, L.; Meziani, M. J.; Sahu, S.; Sun, Y.-P. Photoluminescence Properties of Graphene *versus* Other Carbon Nanomaterials. *Acc. Chem. Res.* **2013**, *46*, 171–180.
(84) Song, Y.; Zhu, S.; Yang, B. Bioimaging Based on Fluorescent Carbon Dots. *RSC Adv.* **2014**, *4*, 27184–27200.
(85) Zheng, Y.; Xie, G.; Zhang, X.; Chen, Z.; Cai, Y.; Yu, W.; Liu, H.; Shan, J.; Li, R.; Liu, Y.; Lei, B. Bioimaging Application and Growth-Promoting Behavior of Carbon Dots from Pollen on

Hydroponically Cultivated Rome Lettuce. *ACS Omega* **2017**, *2*, 3958–3965.
(86) Qian, K.; Guo, H.; Chen, G.; Ma, C.; Xing, B. Distribution of Different Surface Modified Carbon Dots in Pumpkin Seedlings. *Sci. Rep.* **2018**, *8*, 7991.
(87) Torney, F.; Trewyn, B. G.; Lin, V. S.-Y.; Wang, K. Mesoporous Silica Nanoparticles Deliver DNA and Chemicals into Plants. *Nat. Nanotechnol.* **2007**, *2*, 295–300.
(88) Chang, F.-P.; Kuang, L.-Y.; Huang, C.-A.; Jane, W.-N.; Hung, Y.; Hsing, Y.-I. C.; Mou, C.-Y. A Simple Plant Gene Delivery System Using Mesoporous Silica Nanoparticles as Carriers. *J. Mater. Chem. B Mater. Biol. Med.* **2013**, *1*, 5279–5287.
(89) Martin-Ortigosa, S.; Peterson, D. J.; Valenstein, J. S.; Lin, V. S.-Y.; Trewyn, B. G.; Lyznik, L. A.; Wang, K. Mesoporous Silica Nanoparticle-Mediated Intracellular Cre Protein Delivery for Maize Genome Editing *via* loxP Site Excision. *Plant Physiol.* **2014**, *164*, 537–547.
(90) Rastogi, A.; Tripathi, D. K.; Yadav, S.; Chauhan, D. K.; Živčák, M.; Ghorbanpour, M.; El-Sheery, N. I.; Brestic, M. Application of Silicon Nanoparticles in Agriculture. *3 Biotech* **2019**, *9*, 90.
(91) Lin, B.-S.; Diao, S.-Q.; Li, C.-H.; Fang, L.-J.; Qiao, S.-C.; Yu, M. Effect of TMS (Nanostructured Silicon Dioxide) on Growth of Changbai Larch Seedlings. *Res. J. For.* **2004**, *15*, 138–140.
(92) Siddiqui, M. H.; Al-Whaibi, M. H. Role of Nano-SiO_2 in Germination of Tomato (*Lycopersicum esculentum* Seeds Mill.). *Saudi J. Biol. Sci.* **2014**, *21*, 13–17.
(93) Spielman-Sun, E.; Avellan, A.; Bland, G. D.; Tappero, R. V.; Acerbo, A. S.; Unrine, J. M.; Giraldo, J. P.; Lowry, G. V. Nanoparticle Surface Charge Influences Translocation and Leaf Distribution in Vascular Plants with Contrasting Anatomy. *Environ. Sci.: Nano* **2019**, *6*, 2508–2519.
(94) Raven, P. H.; Eichhorn, S. E.; Evert, R. F. *Biology of Plants, 7th ed.;* W.H. Freeman and Company: New York, 2005.
(95) Benedict, C. R.; McCree, K. J.; Kohel, R. J. High Photosynthetic Rate of a Chlorophyll Mutant of Cotton. *Plant Physiol.* **1972**, *49*, 968–971.
(96) Maroco, J. P.; Edwards, G. E.; Ku, M. S. Photosynthetic Acclimation of Maize to Growth under Elevated Levels of Carbon Dioxide. *Planta* **1999**, *210*, 115–125.
(97) Buick, R. D.; Buchan, G. D.; Field, R. J. The Role of Surface Tension of Spreading Droplets in Absorption of a Herbicide Formulation *via* Leaf Stomata. *Pestic. Sci.* **1993**, *38*, 227–235.
(98) Field, R. J.; Bishop, N. G. Promotion of Stomatal Infiltration of Glyphosate by an Organosilicone Surfactant Reduces the Critical Rainfall Period. *Pestic. Sci.* **1988**, *24*, 55–62.
(99) Stevens, P. J. G. Organosilicone Surfactants as Adjuvants for Agrochemicals. *Pestic. Sci.* **1993**, *38*, 103–122.
(100) Castro, M. J. L.; Ojeda, C.; Cirelli, A. F. Surfactants in Agriculture. In *Green Materials for Energy, Products and Depollution*; Lichtfouse, E., Schwarzbauer, J., Robert, D., Eds; Springer Netherlands: Dordrecht, 2013; pp 287–334.
(101) Knoche, M. Organosilicone Surfactant Performance in Agricultural Spray Application: A Review. *Weed Res.* **1994**, *34*, 221–239.
(102) Castro, M. J. L.; Ojeda, C.; Cirelli, A. F. Advances in Surfactants for Agrochemicals. *Environ. Chem. Lett.* **2014**, *12*, 85–95.
(103) Avellan, A.; Yun, J.; Zhang, Y.; Spielman-Sun, E.; Unrine, J. M.; Thieme, J.; Li, J.; Lombi, E.; Bland, G.; Lowry, G. V. Nanoparticle Size and Coating Chemistry Control Foliar Uptake Pathways, Translocation, and Leaf-To-Rhizosphere Transport in Wheat. *ACS Nano* **2019**, *13*, 5291-5305
(104) Bao, W.; Wang, J.; Wang, Q.; O'Hare, D.; Wan, Y. Layered Double Hydroxide Nanotransporter for Molecule Delivery to Intact Plant Cells. *Sci. Rep.* **2016**, *6*, 26738.
(105) Zeiger, E. The Biology of Stomatal Guard Cells. *Annu. Rev. Plant Physiol.* **1983**, *34*, 441–474.
(106) Araújo, W. L.; Fernie, A. R.; Nunes-Nesi, A. Control of Stomatal Aperture: A Renaissance of the Old Guard. *Plant Signal. Behav.* **2011**, *6*, 1305–1311.
(107) McLachlan, D. H.; Kopischke, M.; Robatzek, S. Gate Control: Guard Cell Regulation by Microbial Stress. *New Phytol.* **2014**, *203*, 1049–1063.
(108) Geilfus, C.-M. The pH of the Apoplast: Dynamic Factor with Functional Impact Under Stress. *Mol. Plant* **2017**, *10*, 1371–1386.

(109) Wu, H.; Shabala, L.; Liu, X.; Azzarello, E.; Zhou, M.; Pandolfi, C.; Chen, Z.-H.; Bose, J.; Mancuso, S.; Shabala, S. Linking Salinity Stress Tolerance with Tissue-Specific Na^+ Sequestration in Wheat Roots. *Front. Plant Sci.* **2015**, *6*, 71.
(110) Dunn, K. W.; Kamocka, M. M.; McDonald, J. H. A Practical Guide to Evaluating Colocalization in Biological Microscopy. *Am. J. Physiol. Cell Physiol.* **2011**, *300*, C723–C742.
(111) Williams, W. E.; Gorton, H. L.; Witiak, S. M. Chloroplast Movements in the Field. *Plant Cell Environ.* **2003**, *26*, 2005–2014.
(112) Trojan, A.; Gabrys, H. Chloroplast Distribution in *Arabidopsis thaliana* (L.) Depends on Light Conditions during Growth. *Plant Physiol.* **1996**, *111*, 419–425.
(113) Wada, M. Chloroplast Movement. *Plant Sci.* **2013**, *210*, 177–182.
(114) Lin, J.; Alexander-Katz, A. Cell Membranes Open "Doors" for Cationic Nanoparticles/Biomolecules: Insights into Uptake Kinetics. *ACS Nano* **2013**, *7*, 10799–10808.
(115) Chen, J.; Hessler, J. A.; Putchakayala, K.; Panama, B. K.; Khan, D. P.; Hong, S.; Mullen, D. G.; Dimaggio, S. C.; Som, A.; Tew, G. N.; Lopatin, A. N.; Baker, J. R.; Holl, M. M. B.; Orr, B. G. Cationic Nanoparticles Induce Nanoscale Disruption in Living Cell Plasma Membranes. *J. Phys. Chem. B* **2009**, *113*, 11179–11185.
(116) Rui, Y.; Chen, Y.; Kandemir, B.; Yi, H.; Wang, J. Z.; Puri, V. M.; Anderson, C. T. Balancing Strength and Flexibility: How the Synthesis, Organization, and Modification of Guard Cell Walls Govern Stomatal Development and Dynamics. *Front. Plant Sci.* **2018**, *9*, 1202.
(117) Freudling, C.; Starrach, N.; Flach, D.; Gradmann, D.; Mayer, W. E. Cell Walls as Reservoirs of Potassium Ions for Reversible Volume Changes of Pulvinar Motor Cells during Rhythmic Leaf Movements. *Planta* **1988**, *175*, 193–203.
(118) Wolterbeek, H. T. Cation Exchange in Isolated Xylem Cell Walls of Tomato. I. Cd^{2+} and Rb^+ Exchange in Adsorption Experiments. *Plant Cell Environ.* **1987**, *10*, 39–44.
(119) Lundqvist, M.; Stigler, J.; Elia, G.; Lynch, I.; Cedervall, T.; Dawson, K. A. Nanoparticle Size and Surface Properties Determine the Protein Corona with Possible Implications for Biological Impacts. *Proc. Natl. Acad. Sci. U. S. A.* **2008**, *105*, 14265–14270.
(120) Monopoli, M. P.; Walczyk, D.; Campbell, A.; Elia, G.; Lynch, I.; Bombelli, F. B.; Dawson, K. A. Physical-Chemical Aspects of Protein Corona: Relevance to *In Vitro* and *In Vivo* Biological Impacts of Nanoparticles. *J. Am. Chem. Soc.* **2011**, *133*, 2525–2534.
(121) Durán, N.; Silveira, C. P.; Durán, M.; Martinez, D. S. T. Silver Nanoparticle Protein Corona and Toxicity: A Mini-Review. *J. Nanobiotechnology* **2015**, *13*, 55.
(122) Barbir, R.; Goessler, W.; Ćurlin, M.; Micek, V.; Milić, M.; Vuković, B.; Milić, M.; Ljubojević, M.; Domazet Jurašin, D.; Vinković Vrček, I. Protein Corona Modulates Distribution and Toxicological Effects of Silver Nanoparticles *In Vivo*. *Part. Part. Syst. Charact.* **2019**, *18*, 1900174.
(123) Pitek, A. S.; Wen, A. M.; Shukla, S.; Steinmetz, N. F. The Protein Corona of Plant Virus Nanoparticles Influences Their Dispersion Properties, Cellular Interactions, and *In Vivo* Fates. *Small* **2016**, *12*, 1758–1769.
(124) Ponnuvel, S.; Subramanian, B.; Ponnuraj, K. Conformational Change Results in Loss of Enzymatic Activity of Jack Bean Urease on Its Interaction with Silver Nanoparticle. *Protein J.* **2015**, *34*, 329–337.
(125) Yamaoka, K.; Nakagawa, T.; Uno, T. Statistical Moments in Pharmacokinetics. *J. Pharmacokinet. Biopharm.* **1978**, *6*, 547–558.
(126) Shargel, L.; Wu-Pong, S.; Yu, A. *Applied Biopharmaceutics & Pharmacokinetics, Fifth Edition;* McGraw Hill Professional: New York, 2004; pp 1–30.
(127) Gibaldi, M. *Compartmental and Noncompartmental Pharmacokinetics, Fourth edition;* Lea & Feiber Philadelphia: Malvern, PA, 1991; pp 1–13.
(128) Andes, D.; Craig, W. A. Animal Model Pharmacokinetics and Pharmacodynamics: A Critical Review. *Int. J. Antimicrob. Agents* **2002**, *19*, 261–268.
(129) Graham, M. A.; Lockwood, G. F.; Greenslade, D.; Brienza, S.; Bayssas, M.; Gamelin, E. Clinical Pharmacokinetics of Oxaliplatin: A Critical Review. *Clin. Cancer Res.* **2000**, *6*, 1205–1218.

(130) Glass, P. S. A.; Gan, T. J.; Howell, S. A Review of the Pharmacokinetics and Pharmacodynamics of Remifentanil. *Anesthesia & Analgesia* **1999**, *89*, 7–14.

(131) Khan, W. U.; Wang, D.; Zhang, W.; Tang, Z.; Ma, X.; Ding, X.; Du, S.; Wang, Y. High Quantum Yield Green-Emitting Carbon Dots for Fe(III) Detection, Biocompatible Fluorescent Ink and Cellular Imaging. *Sci. Rep.* **2017**, *7*, 14866.

(132) Asati, A.; Santra, S.; Kaittanis, C.; Nath, S.; Perez, J. M. Oxidase-like Activity of Polymer-Coated Cerium Oxide Nanoparticles. *Angew. Chem. Int. Ed Engl.* **2009**, *48*, 2308–2312.

(133) Collin, B.; Oostveen, E.; Tsyusko, O. V.; Unrine, J. M. Influence of Natural Organic Matter and Surface Charge on the Toxicity and Bioaccumulation of Functionalized Ceria Nanoparticles in *Caenorhabditis elegans*. *Environ. Sci. Technol.* **2014**, *48*, 1280–1289.

(134) Asati, A.; Santra, S.; Kaittanis, C.; Perez, J. M. Surface-Charge-Dependent Cell Localization and Cytotoxicity of Cerium Oxide Nanoparticles. *ACS Nano* **2010**, *4*, 5321–5331.

(135) Larson, D. R.; Ow, H.; Vishwasrao, H. D.; Heikal, A. A.; Wiesner, U.; Webb, W. W. Silica Nanoparticle Architecture Determines Radiative Properties of Encapsulated Fluorophores. *Chem. Mater.* **2008**, *20*, 2677–2684.

(136) Lowry, G. V.; Hill, R. J.; Harper, S.; Rawle, A. F. Guidance to Improve the Scientific Value of Zeta-Potential Measurements in nanoEHS. *Environmentalist* **2016**, *3*, 953–965.

(137) Doane, T. L.; Chuang, C.-H.; Hill, R. J.; Burda, C. Nanoparticle ζ -Potentials. *Acc. Chem. Res.* **2012**, *45*, 317–326.

(138) Skoglund, S.; Hedberg, J.; Yunda, E.; Godymchuk, A.; Blomberg, E.; Odnevall Wallinder, I. Difficulties and Flaws in Performing Accurate Determinations of Zeta Potentials of Metal Nanoparticles in Complex Solutions-Four Case Studies. *PLoS One* **2017**, DOI.10.1371/journal.pone.0181735

(139) Pradhan Mitra, P.; Loqué, D. Histochemical Staining of *Arabidopsis thaliana* Secondary Cell Wall Elements. *J. Vis. Exp.* **2014**, DOI.org/10.3791/51381.

(140) Jelínková, A.; Malínská, K.; Simon, S.; Kleine-Vehn, J.; Parezová, M.; Pejchar, P.; Kubes, M.; Martinec, J.; Friml, J.; Zazímalová, E.; Petrásek, J. Probing Plant Membranes with FM Dyes: Tracking, Dragging or Blocking? *Plant J.* **2010**, *61*, 883–892.

(141) Emans, N.; Zimmermann, S.; Fischer, R. Uptake of a Fluorescent Marker in Plant Cells Is Sensitive to Brefeldin A and Wortmannin. *Plant Cell* **2002**, *14*, 71–86.

(142) Bolte, S.; Talbot, C.; Boutte, Y.; Catrice, O.; Read, N. D.; Satiat-Jeunemaitre, B. FM-Dyes as Experimental Probes for Dissecting Vesicle Trafficking in Living Plant Cells. *J. Microsc.* **2004**, *214*, 159–173.

(143) Mullineaux, D. R. CI2 for Creating and Comparing Confidence-Intervals for Time-Series Bivariate Plots. *Gait Posture* **2017**, *52*, 367–373.

(144) Zaiontz, C. Confidence Ellipse Analysis Tool, 2019. Real Statistics Using Excel. https://www.real-statistics.com/multivariate-statistics/multivariate-normal-distribution/confidence-ellipse-analysis-tool/ (accessed March 8, 2020)

Table of Content

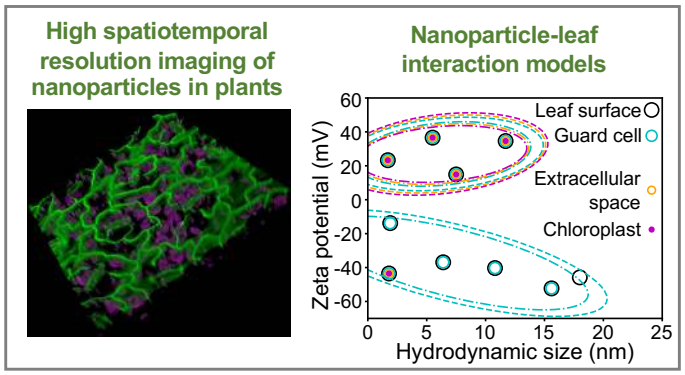

Figure 1

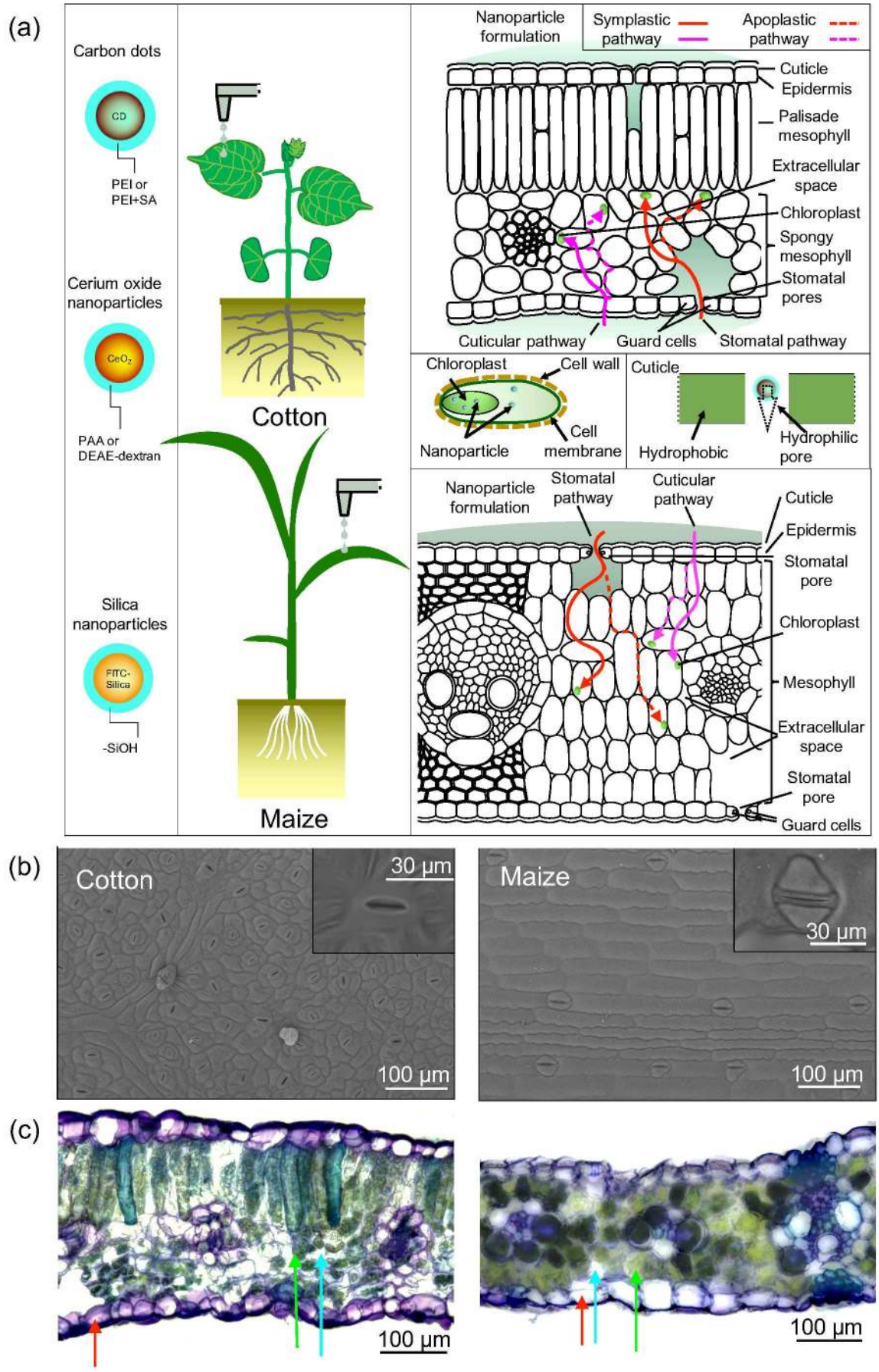
(a)
Carbon dots
CD
PEI or PEI+SA
Cerium oxide nanoparticles
CeO2
PAA or DEAE-dextran
Silica nanoparticles
FITC-Silica
-SiOH
Cotton
Maize
Nanoparticle formulation
Symplastic pathway
Apoplastic pathway
Cuticle
Epidermis
Palisade mesophyll
Extracellular space
Chloroplast
Spongy mesophyll
Stomatal pores
Cuticular pathway
Guard cells
Stomatal pathway
Chloroplast
Cell wall
Nanoparticle
Cell membrane
Cuticle
Hydrophobic
Hydrophilic pore
Nanoparticle formulation
Stomatal pathway
Cuticular pathway
Cuticle
Epidermis
Stomatal pore
Chloroplast
Mesophyll
Extracellular space
Stomatal pore
Guard cells
(b)
Cotton
30 μm
100 μm
Maize
30 μm
100 μm
(c)
100 μm
100 μm

Figure 2

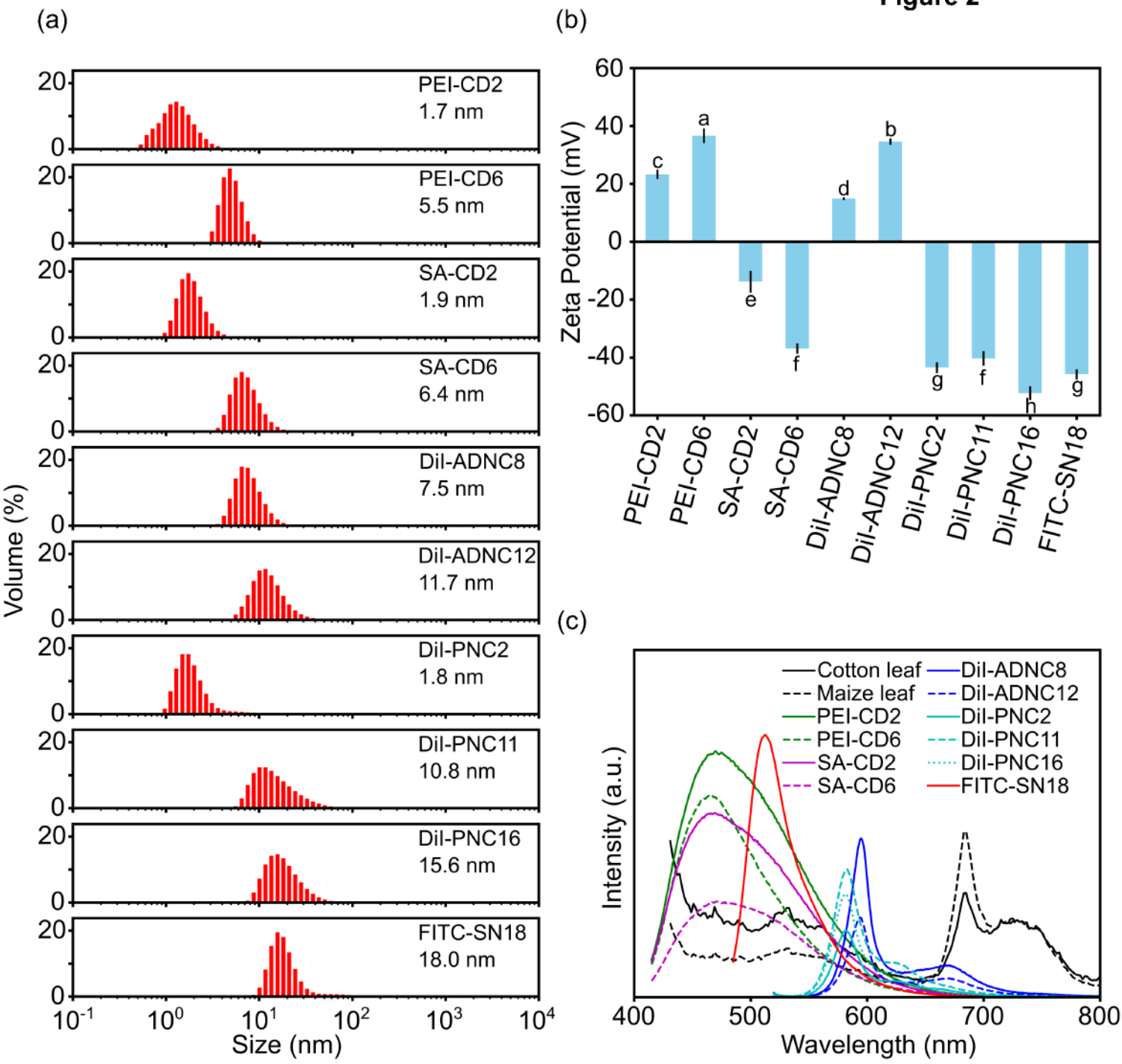
(a)
PEI-CD2
1.7 nm
PEI-CD6
5.5 nm
SA-CD2
1.9 nm
SA-CD6
6.4 nm
DiI-ADNC8
7.5 nm
DiI-ADNC12
11.7 nm
DiI-PNC2
1.8 nm
DiI-PNC11
10.8 nm
DiI-PNC16
15.6 nm
FITC-SN18
18.0 nm
Volume (%)
Size (nm)
(b)
Zeta Potential (mV)
PEI-CD2
PEI-CD6
SA-CD2
SA-CD6
DiI-ADNC8
DiI-ADNC12
DiI-PNC2
DiI-PNC11
DiI-PNC16
FITC-SN18
(c)
Cotton leaf
Maize leaf
PEI-CD2
PEI-CD6
SA-CD2
SA-CD6
DiI-ADNC8
DiI-ADNC12
DiI-PNC2
DiI-PNC11
DiI-PNC16
FITC-SN18
Intensity (a.u.)
Wavelength (nm)

Figure 3

(a)

Leaf NP uptake

No leaf NP uptake

	Cotton				Maize			
	PEI-CD2	SA-CD2	PEI-CD6	SA-CD6	PEI-CD2	SA-CD2	PEI-CD6	SA-CD6
Triton X-100								
Silwet L-77								

(b)

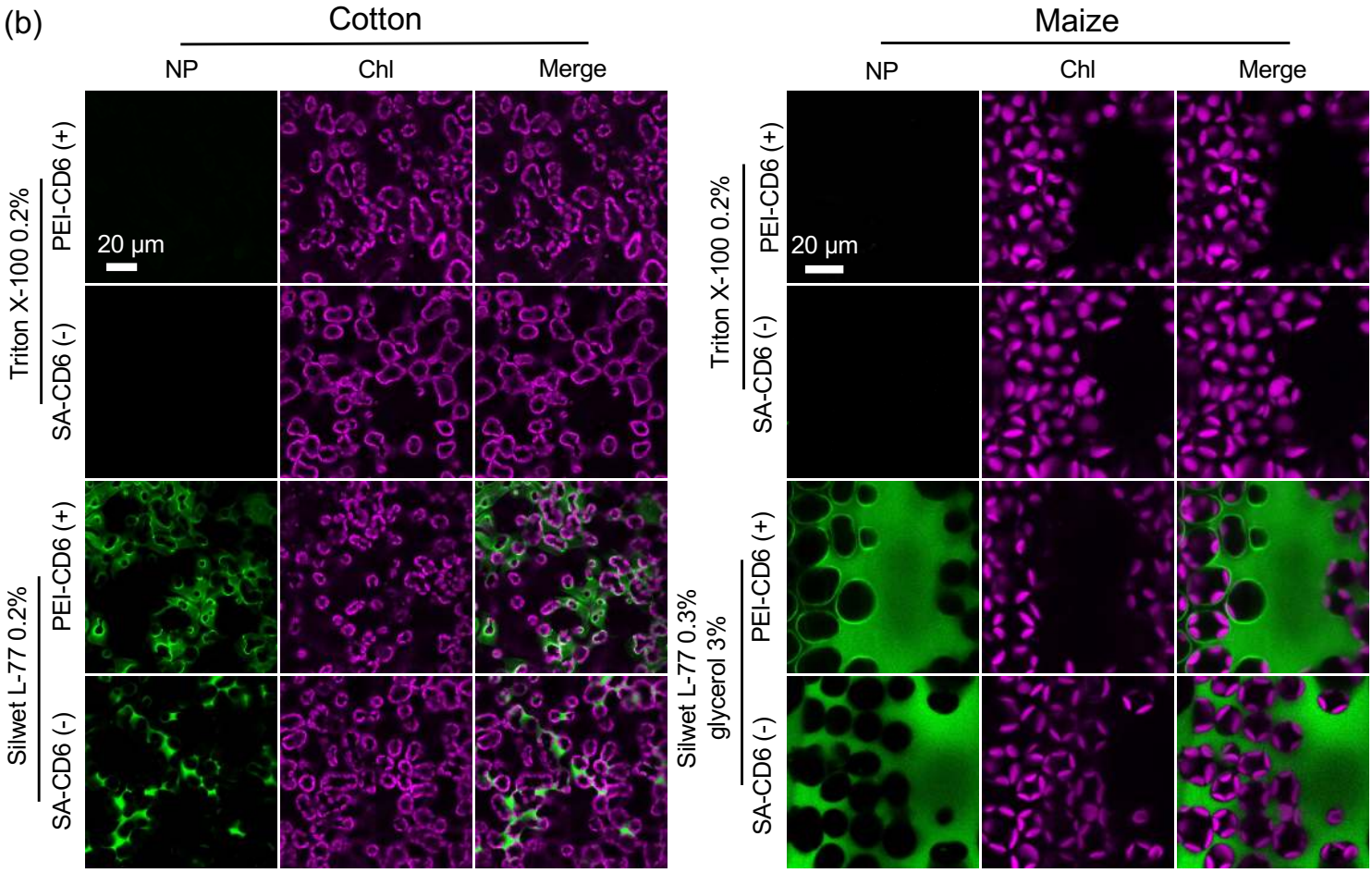

Figure 4

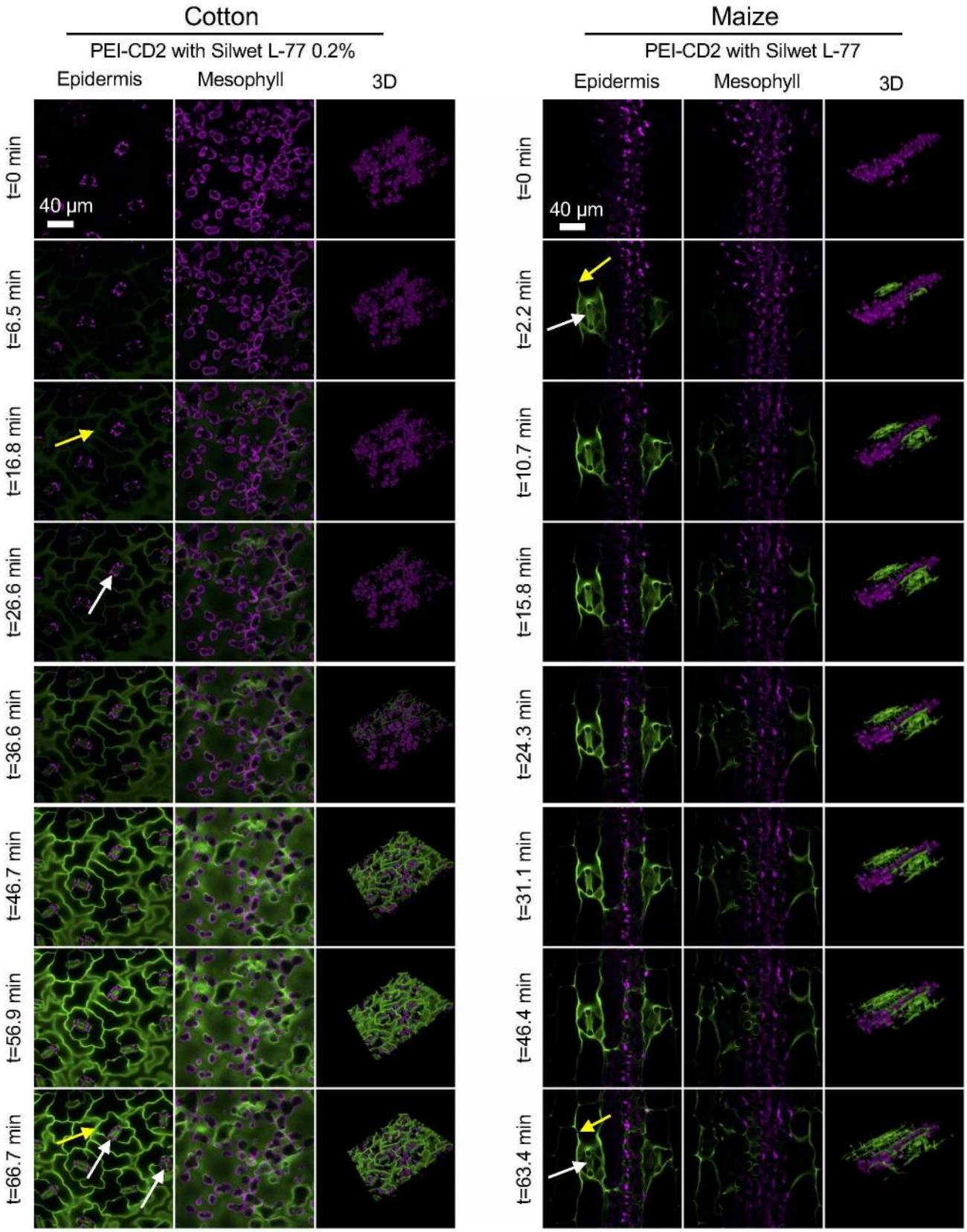
Cotton
PEI-CD2 with Silwet L-77 0.2%
Epidermis
Mesophyll
3D
Maize
PEI-CD2 with Silwet L-77
Epidermis
Mesophyll
3D
t=0 min
t=6.5 min
t=16.8 min
t=26.6 min
t=36.6 min
t=46.7 min
t=56.9 min
t=66.7 min
t=0 min
t=2.2 min
t=10.7 min
t=15.8 min
t=24.3 min
t=31.1 min
t=46.4 min
t=63.4 min
40 µm
40 µm

Figure 5

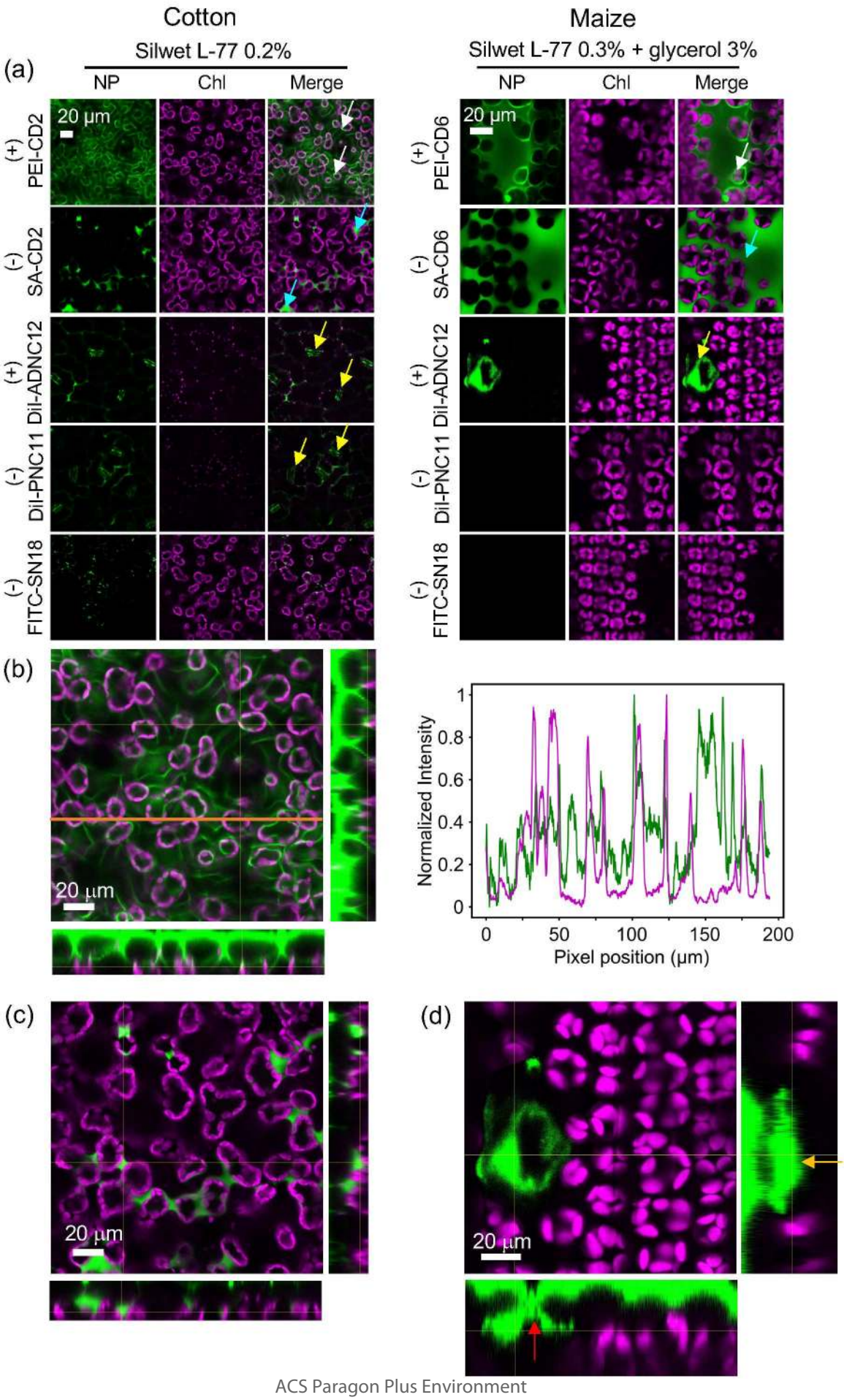
Cotton
Silwet L-77 0.2%
Maize
Silwet L-77 0.3% + glycerol 3%
(a)
NP
Chl
Merge
20 μm
(+) PEI-CD2
(-) SA-CD2
(+) DiI-ADNC12
(-) DiI-PNC11
(-) FITC-SN18
(+) PEI-CD6
(-) SA-CD6
(+) DiI-ADNC12
(-) DiI-PNC11
(-) FITC-SN18
(b)
20 μm
Normalized Intensity
Pixel position (μm)
(c)
20 μm
(d)
20 μm

Figure 6

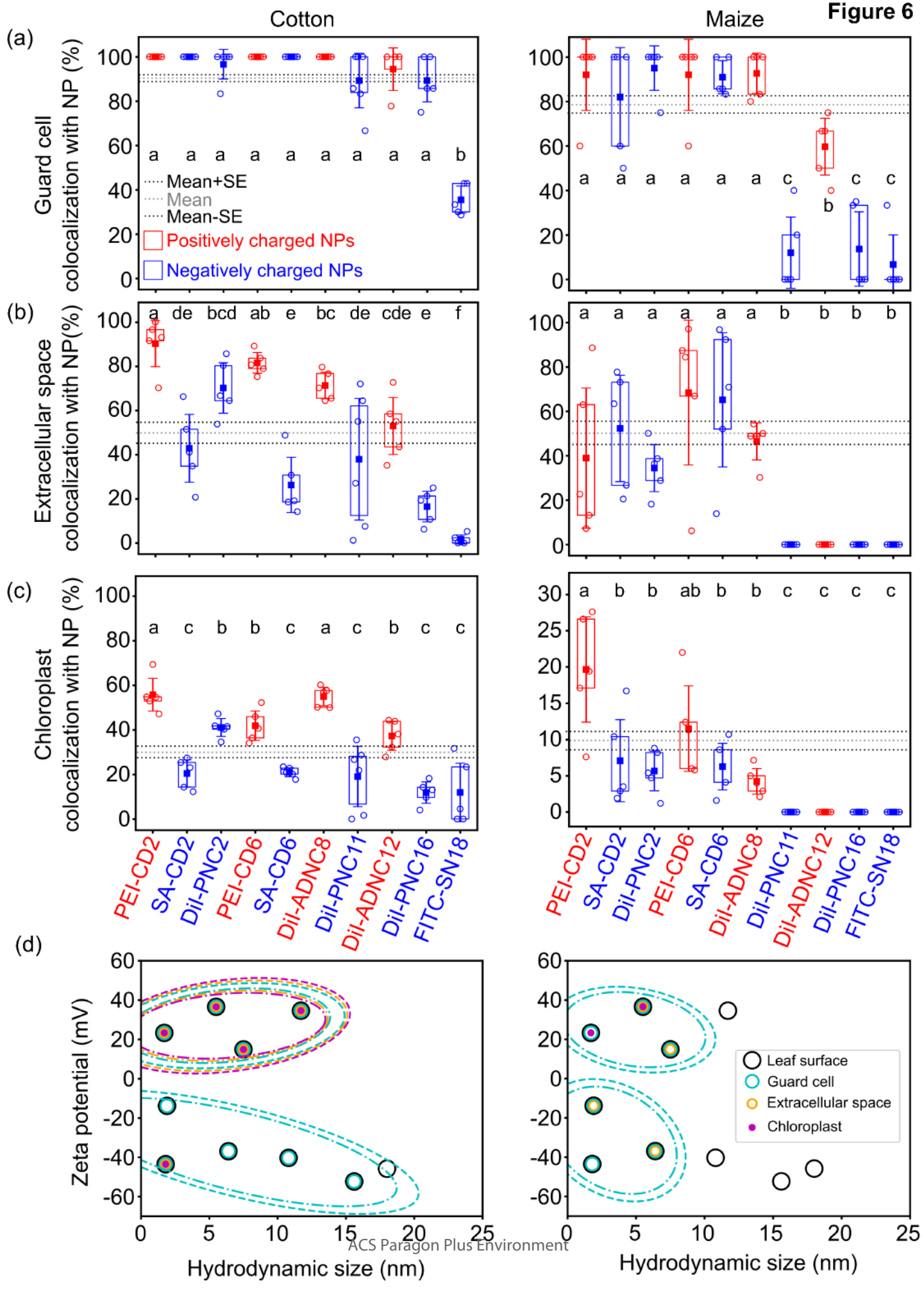
Cotton
Maize
(a)
Guard cell colocalization with NP (%)
Mean+SE
Mean
Mean-SE
Positively charged NPs
Negatively charged NPs
(b)
Extracellular space colocalization with NP(%)
(c)
Chloroplast colocalization with NP (%)
PEI-CD2
SA-CD2
DiI-PNC2
PEI-CD6
SA-CD6
DiI-ADNC8
DiI-PNC11
DiI-ADNC12
DiI-PNC16
FITC-SN18
(d)
Zeta potential (mV)
Hydrodynamic size (nm)
Leaf surface
Guard cell
Extracellular space
Chloroplast